11-29-2018

The Effect of Near-Spark-Plug Flow Field on Spark Discharge Characteristics

Navjot S. Sandhu
University of Windsor

The Effect of Near-Spark-Plug Flow Field on Spark Discharge Characteristics

by

Navjot S. Sandhu

A Thesis
Submitted to the Faculty of Graduate Studies
through Mechanical, Automotive, and Materials Engineering
in Partial Fulfillment of the Requirements for
the Degree of Master of Applied Science at the
University of Windsor

Windsor, Ontario, Canada

The Effect of Near-Spark-Plug Flow Field on Spark Discharge Characteristics

by

Navjot S. Sandhu

APPROVED BY:

_____

X. Chen

Department of Electrical and Computer Engineering

_____

N. Eaves

Department of Mechanical, Automotive, and Materials Engineering

_____

M. Zheng, Co-Advisor

Department of Mechanical, Automotive, and Materials Engineering

_____

D. Ting, Co-Advisor

Department of Mechanical, Automotive, and Materials Engineering

29 November, 2018

AUTHOR'S DECLARATION OF ORIGINALITY

I hereby certify that I am the sole author of this thesis and that no part of this thesis has been published or submitted for publication.

I certify that, to the best of my knowledge, my thesis does not infringe upon anyone's copyright nor violate any proprietary rights and that any ideas, techniques, quotations, or any other material from the work of other people included in my thesis, published or otherwise, are fully acknowledged in accordance with the standard referencing practices. Furthermore, to the extent that I have included copyrighted material that surpasses the bounds of fair dealing within the meaning of the Canada Copyright Act, I certify that I have obtained a written permission from the copyright owner(s) to include such material(s) in my thesis and have included copies of such copyright clearances to my appendix.

I declare that this is a true copy of my thesis, including any final revisions, as approved by my thesis committee and the Graduate Studies office, and that this thesis has not been submitted for a higher degree to any other University or Institution.

ABSTRACT

Advanced spark ignition (SI) engines can operate under lean conditions in order to improve the efficiency and reduce the emissions. Under extensive lean conditions, the ignition and complete combustion of the charge mixture is a challenge, because of the reduced cylinder charge reactivity. The enhancement of the in-cylinder global motion and local turbulence is an effective way to increase the flame velocity, and consequently shorten the combustion duration. The role of air motion in improving air-fuel mixing and combustion has been researched extensively. However, during the ignition process, the excessive charge motion can hinder the spark discharge, the resulting flame kernel formation and propagation. Therefore, a combined empirical and simulation study is undertaken to elucidate the flow field around the spark gap, and its effect on the spark discharge. The flow field generated by a steady flow of air across the spark gap of a conventional J-type spark plug is studied under ambient conditions. Optical particle image velocimetry (PIV) measurements and computational fluid dynamics (CFD) simulations are performed alongside the high-speed direct imaging. Voltage and current waveforms of the spark channel have been measured, in order to correlate the spark behavior to the local flow velocity. The flow field near the spark gap in an SI engine under motoring conditions is simulated. The results are compared to the empirical current and voltage measurements taken during engine operation. The results show that the turbulence is generated in the wake of the spark plug and flow velocity in the spark gap is higher than the free stream velocity. The optical and electrical measurements show the spark stretching and restrikes increase, and the discharge duration decreases with an increase in flow velocity. Similar behavior is observed during engine operation as well.

DEDICATION

This thesis is dedicated to loving family.

My Parents S. Jaswinder Singh and Palwinder Kaur, and my sister Samreet.

ACKNOWLEDGEMENTS

Firstly, I would like to thank my advisors, Dr. Ming Zheng and Dr. David Ting, for giving me the opportunity to perform research within this laboratory and for providing me with continuous guidance and support in my studies and research. I would also like to acknowledge my committee members Dr. Xiang Chen and Dr. Nick Eaves for their advice and perspective on my research.

I would also like to extend my appreciation to my colleagues in the Clean Combustion Engine Laboratory. Countless conversations and encouraging advice from Dr. Meiping Wang, Dr. Shui Yu, Dr. Xiao Yu, Dr. Tadanori Yanai, Dr. Prasad Divekar, Dr. Tongyang Gao, Dr. Shouvik Dev, Dr. Kelvin Xie, Qingyuan Tan, Zhenyi Yang, Christopher Aversa, Geraint Bryden, Mark Ives, Zhu Hua, Divyanshu Purohit, Liang Li, Linyan Wang, Chang Ye and Akshay Ravi have given me a unique perspective on different areas of research as well as various experimental procedures. It has been a pleasure working with you all.

I would like to thank Mr. Bruce Durfy, who greatly assisted me with the fabrication of many laboratory components both for my research and for use in other areas of the lab.

A special thanks is also extended to the following organizations for their funding support: The University of Windsor, the NSERC Industrial Research Chair program, NSERC Collaborative Research and development Program, Ontario Center of Excellency – VIP II program, Ford Motor Company of Canada Ltd.

TABLE OF CONTENTS

LIST OF TABLES

LIST OF FIGURES

LIST OF NOMENCLATURE

AMR	Adaptive Mesh Refinement	
CA	Crank Angle	[°]
CAA	Clean Air Act	
CAFE	Corporate Average Fuel Economy	[mpg]
CARB	California Air Research Board	
CCEL	Clean Combustion Engine Laboratory	
CFD	Computational Fluid Dynamics	
CMOS	Complementary Metal-Oxide Semiconductor	
CO	Carbon Monoxide	
d	hydraulic diameter	[m]
DAQ	Data Acquisition	
DC	Direct Current	
DOC	Diesel Oxidation Catalyst	
EGR	Exhaust Gas Recirculation	
EPA	Environment Protection Agency	
EVC	Exhaust Valve Closing	[° CA]
EVO	Exhaust Valve Opening	[° CA]
FFT	Fast Fourier Transformation	
FPGA	Field Programmable Gate Array	
fps	frames per second	
GHG	Green-House Gas	
HC	Hydrocarbon	

IGBT	Insulated Gate Bipolar Transistor	
IVC	Inlet Valve Closing	[° CA]
IVO	Inlet Valve Opening	[° CA]
IW	Interrogation Window	
k	turbulent kinetic energy	[J]
LDV	Laser Doppler Velocimetry	
MAF	Mass Air Flow	[g/s]
Nd-YAG	Neodymium-doped Yttrium Aluminum Garnet	
NI	National Instruments	
NOx	Nitrogen Oxides	
PIV	Particle Image Velocimetry	
PM	Particulate Matter	
px	pixels	
Re	Reynolds Number	
RNG	Renormalized Group	
rpm	revolutions per minute	
RT	Real Time	
SI	Spark Ignition	
TDC	Top Dead Center	
TCI	Transistor Coil Ignition	
u’	turbulent velocity	[m/s]
$\bar{U}$	mean flow velocity	[m/s]
US	United States	

$\bar{V}$	velocity	[m/s]
V_{max}	maximum particle velocity	[m/s]
V_{min}	minimum particle velocity	[m/s]
$\Delta\bar{X}$	particle displacement	[m]
Δt	time between laser pulses	[s]
ε	dissipation rate	$[m^2/s^3]$
μ	dynamic viscosity	$[m^2/s]$
ρ	density	$[kg/m^3]$
ω	vorticity	$[s^{-1}]$

INTRODUCTION

Gasoline fueled, spark ignition (SI) internal combustion engines constitute a major portion of powertrains for the light duty passenger and goods transport vehicles. Even with battery powered vehicles receiving significant attention in recent years, gasoline powered non-hybrid SI vehicles accounted for 97% of total light duty vehicle sales in the year 2016 in United States [1,2]. Thus, improving the fuel economy while meeting strict emission standards is the focus of SI engine research. In this chapter, the research motivation, background and associated challenges pertaining to the author's research are described. Thereafter, an outline of the thesis structure is presented.

1.1 Research Motivation

Since the early 1970's, government agencies like the United States' Environment Protection Agency (US-EPA) and California Air Resources Board (CARB) have set the limits on air pollutants from automotive vehicles following the amendments to Clean Air Act (CAA) of 1970. In the past few decades, the emission legislations are becoming increasingly stringent. Nitrogen oxides (NOx) and carbon monoxide (CO) are the two most regulated constituents of the SI engine exhaust. Cumulative reductions of ~94% in NOx and ~70% in CO emissions have been mandated by the US-EPA [3]. Regulations for green-house gas (GHG) and particulate matter (PM) emissions have also been tightened recently. In addition to the stringent emission standards, vehicle manufacturers are also mandated to meet the corporate average fuel economy (CAFE) standards set to keep fuel economy and CO_2 emissions in check [4,5]. Consequently, the fuel economy of passenger and light duty vehicles has been steadily improving in the past few decades, and this trend is expected to

continue in the future (Figure 1-1). The US federal government recently proposed freezing the fuel economy standards after 2020 citing the cost effectiveness and consumer safety as the main reasons [6]. However, the final verdict on the proposed CAFE standards or any amendments to the same have not yet been given by the US-EPA.

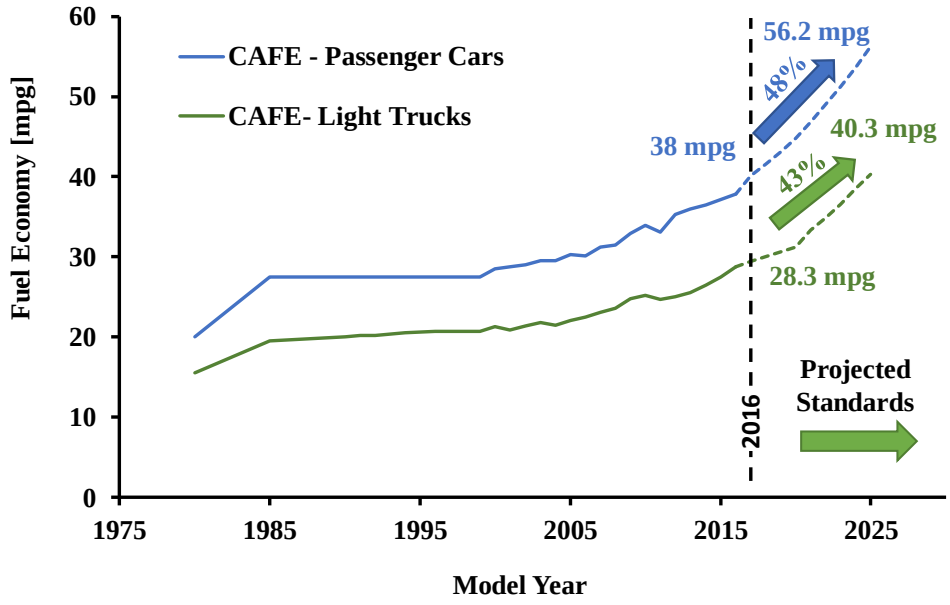

Figure 1-1. CAFE trends and projections for passenger and light-duty vehicles

Hence, continuous improvement in SI engine design and operation can have significant economic and environmental impacts. The main driving factors for future SI engine development are emission reduction and fuel efficiency improvement.

1.2 Lean or Diluted Combustion

Different in-cylinder and exhaust after-treatment strategies have been studied to improve the SI engine efficiency and environmental sustainability [7-19]. The lean or diluted combustion is one of the in-cylinder strategies, which has been proven to be an effective method for improving the efficiency of gasoline SI engines [13-15,19]. The lean and/or diluted combustion can be realized by either increasing the amount of fresh intake air e.g.

by increasing the throttle opening at partial load or by using exhaust gas recirculation (EGR) to dilute the incoming fresh air with a portion of the exhaust gas. The lean or diluted combustion helps reduce the pumping losses associated with the partial load flow restrictions of the throttle body. Excess air increases the burning efficiency and allows a higher compression ratio. Therefore, theoretically lean burn engines should have higher thermal efficiency. In practice; however, lean combustion beyond a certain excess air ratio might lead to incomplete combustion of the in-cylinder charge which results in an increase in unburnt HC and lower fuel efficiency. This limiting condition is called the "lean limit" of the charge mixture. The effect of excess air on combustion performance is illustrated in Figure 1-2.

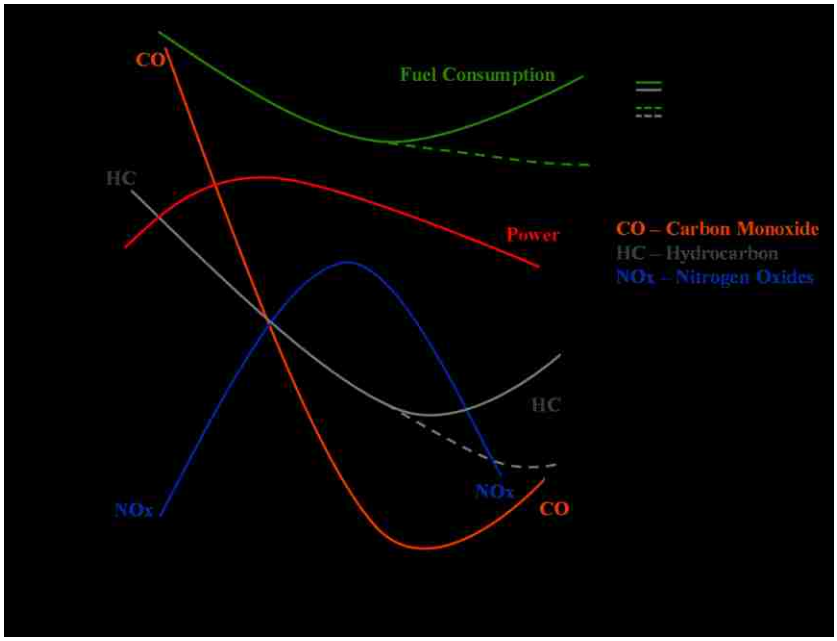

Figure 1-2. Effect of excess air on engine performance (adopted from John [19])

Some possible reasons of the deteriorating performance beyond the lean limit can be the suppression of the charge reactivity and slower burning velocity of excessively lean mixtures [13,20]. Suppressed charge reactivity can reduce the ignitability of the charge,

leading to increased ignition delay. Slower burning velocity in lean mixtures increases the combustion duration [20]. As a result, the combustion might be incomplete by the time the exhaust valve opens. This leads to a fuel consumption penalty and increased hydrocarbon emissions. Further diluting the mixture beyond the lean limit can lead to misfire conditions where the charge is unable to ignite.

1.3 In-Cylinder Charge Motion

One possible strategy to counteract the slower flame speed due to charge dilution is the enhancement of in-cylinder charge motion. In addition to local turbulence, the global flow field can be described by two types of rotational motions, swirl and tumble. The swirl motion is the air/charge rotation around the cylinder axis whereas the tumble is the rotational motion around the axis perpendicular to the cylinder axis. Both swirl and tumble motions increase the turbulence as a result of viscous shear forces between fluid layers. The enhancement of in-cylinder charge motion is an effective way to speed up the flame propagation in SI engines and to extend the lean limit [21]. Typically, the charge motion inside an engine cylinder is controlled by the number of intake ports, port geometry and position, and piston bowl profile [22,23].

Turbulence produced by the charge motion can enhance the flame speed because of the flame front wrinkling effect, which increases the area of contact between burnt and unburnt gases [24]. This phenomenon is illustrated in Figure 1-3 using homogeneous burning of a lean (λ=1.6) methane-air mixture in laminar and turbulence conditions. Both the image frames are taken 25 ms after the ignition event. The turbulent flame propagation is significantly faster than the laminar flame and the wrinkled flame front can be clearly observed.

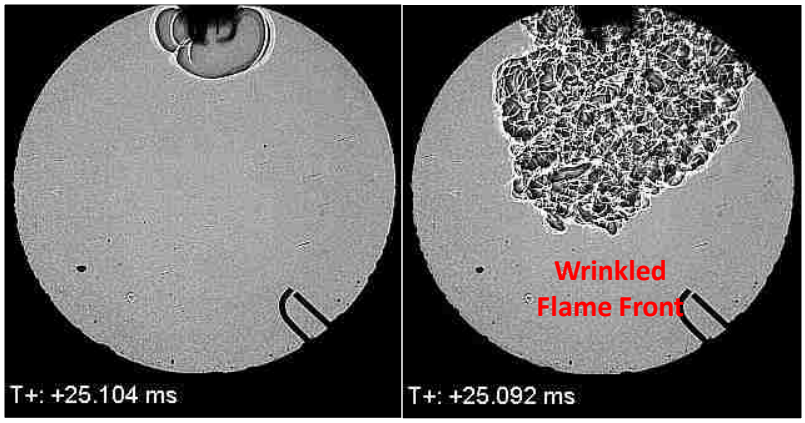

Figure 1-3. Laminar and turbulent methane-air flame front propagation [26]

Although the charge motion helps increase the flame speed and decrease the combustion duration, it can have a significant impact on the spark arcing and early flame kernel formation processes. Once a self-sustaining flame kernel is formed, the flame propagation in SI engines can be enhanced by certain combinations of flow velocity and turbulence in the vicinity of the spark plug [26,33]. However, intense turbulence or very high flow velocity in the early stages of flame kernel formation can lead to misfire.

It has been reported that spark geometry can have a major influence on the local flow velocity and turbulence intensity [26]. Eddies and vortices are often generated in the wake of the spark plug extensions, including the spark electrodes [26,41]. The turbulence near the spark electrodes can influence the flame kernel development and early flame propagation.

1.4 Ignition in SI Engines

The ignition process in SI engines is initiated by the ignition system. The transistor coil ignition (TCI) system is the most widely used ignition system in SI engines owing to its design simplicity, robust performance and cost effectiveness. It mainly consists of a power

supply, an inductive coil pack, a transistor switch or driver and a spark plug (Figure 1-4). The ignition process is initiated by a spark plasma that heats up the combustible mixture across the spark gap. During the initial spark discharging process, a potential difference is applied across the spark plug electrodes resulting in the buildup of an electric field across the spark gap. This electric field accelerates the electrons and ions between the gap which eventually leads to the establishment of a conductive plasma channel connecting the gap. This stage is called the breakdown phase. This phase is followed by the arc phase during which the energy stored in coil, and structure capacitance starts to release. Finally, the discharge process transitions into the glow phase, releasing most of the stored electrical energy. The glow phase is the longest stage of the spark discharge process and thus, it is most liable to the impact of the flow field [22]. The TCI system, and the discharge current and voltage waveforms of a typical spark event is shown in Figure 1-4.

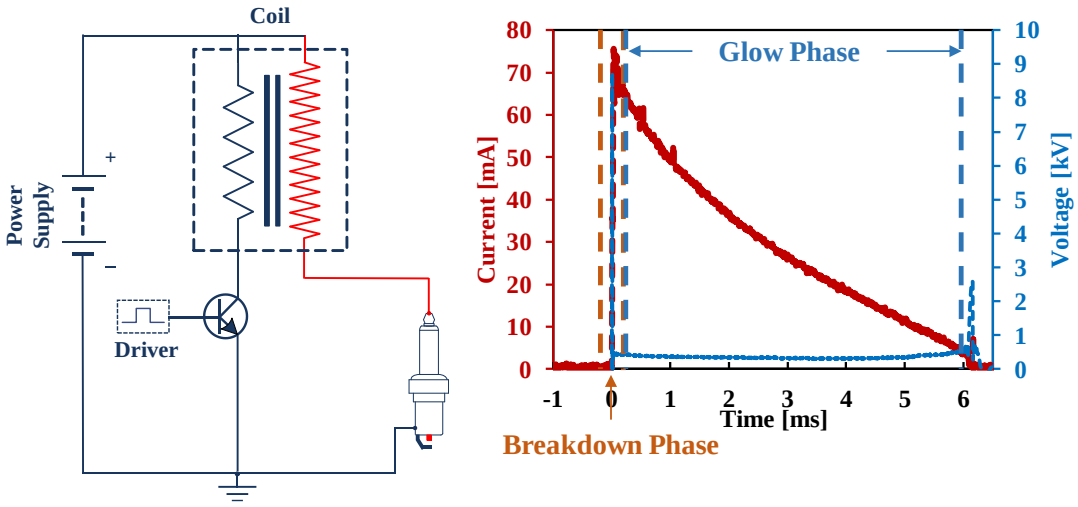

Figure 1-4. TCI spark current and voltage waveforms

Studies have shown that under the flow field effect, the plasma channel during the glow phase tends to deflect or stretch out of the spark gap in the flow direction [27-29]. This elongates the spark as illustrated in Figure 1-5 and provides additional spark length for the

flame kernel formation. The stretching of the spark plasma also increases the gap resistance of the spark channel. Therefore, while this extra spark length can provide additional surface area for flame kernel to develop, the energy density of the spark channel is reduced largely depending on the flow velocity. Consequently, the energy might not be enough to generate a self-sustaining flame. Thereby, the charge mixture can either fail to ignite completely, or a flame kernel can develop and later be extinguished due it its inability to sustain the combustion [30].

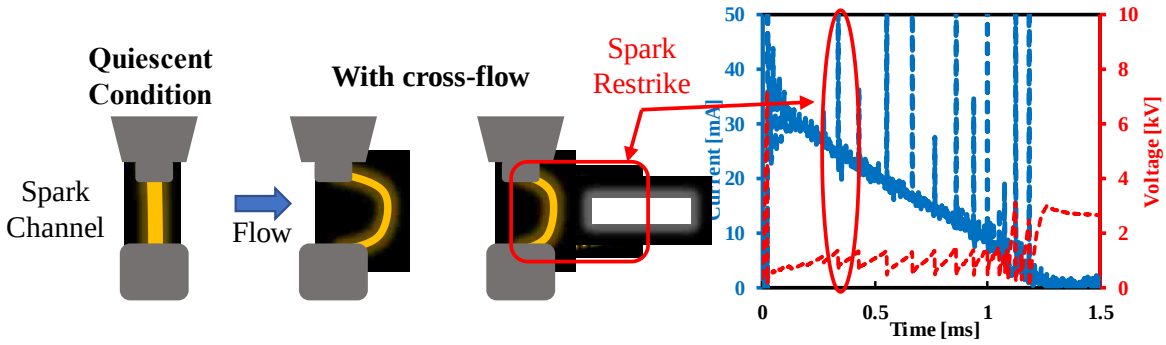

Figure 1-5. Spark channel behavior in flow condition

The stretching beyond a certain length may lead to the breaking of the plasma channel. The gap voltage rises so that the re-establishment of a shorter channel may occur to continue the energy release process across the gap. This event is termed as “restrike”. As illustrated earlier in Figure 1-4, TCI systems have a typical declining discharge current profile. As the current level decays during the discharge process, the frequency of restrikes tends to increase, and thereby the spark channel stretch becomes shorter. The spark stretch may aid the ignition process by partially preventing the heat loss to the relatively cold spark electrodes and extending the plasma channel into unburnt charge mixture. Restrikes cause the plasma to snap back to the spark gap.

Previous research [31,32] indicates that, below a certain current level, the spark plasma remains very close to the spark gap, which inhibits the access to the fresh charge mixture and increases the thermal losses incurred by the flame kernel to the spark electrodes. The spark channel interruptions because of the restrike events can also prevent the formation of a self-sustained flame kernel, forming a “weaker” flame kernel instead. If several of these “weak” spark kernels are formed and later extinguished, the overall ignition process would subsequently fail.

In addition to the spark channel, flow velocity also effects the formed flame kernel. It has been reported that in order for a flame kernel to be self-sustaining, the conductive and radiative losses due to the flow must be compensated by the volumetric burn rate [33]. With longer flame stretch and wrinkling at higher flow velocity, the enlarged surface area increases these losses. It is possible to overcome the effect of flow velocity and turbulence by increasing the initial ignition energy [33]. For a given ignition energy, there may exist a turbulence and velocity threshold beyond which the flame kernel cannot be sustained, early flame propagation may be slowed down or even be extinguished.

1.5 Research Objectives

It is clear from the discussion that the flow velocity has a significant influence on the ignition process and the subsequent flame propagation. The effects of flow velocity can be perceived in two aspects, the turbulence and the spark plasma behaviors. The flow turbulence influences the background conditions for the flame kernel formation, and flame propagation. Whereas, the spark plasma supplies the required energy for the formation of the flame kernel. The turbulence patterns generated or affected by the spark plug geometry can influence the flame propagation and hence, the ignition process. However, the flow

velocity by itself and the spark channel restrikes can have a detrimental effect on the self-sustaining flame kernel formation. Therefore, to obtain a better understanding of the ignition process, the study of flow field near the spark gap and the spark plasma behavior in the flow, is important. In this research, the author attempts to elucidate the aspects of the flow field on the spark ignition process.

The primary objectives of this research include the study of the near-spark-plug flow field and the spark discharge characteristics, especially the steady flow across the spark gap. The flow field in the vicinity of the spark gap under ambient as well as engine motoring conditions is investigated to study the background flow conditions. The spark discharge characteristics of the spark event under steady flow across the spark gap are studied in order to determine the spark plasma response to the flow field. The primary objectives of the research are summarized in Figure 1-6.

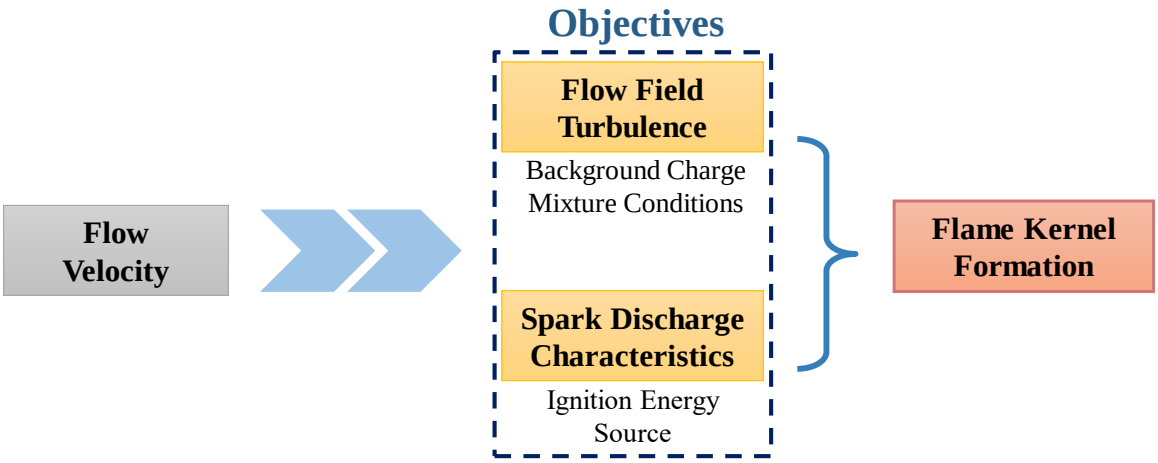

Figure 1-6. Primary research objectives

The secondary objective is to explore the feasibility of using the spark plasma channel response towards the flow field, namely restrike frequency and discharge duration, as a

method of predicting the local flow velocity trends during the spark event in SI engine operation without any optical access into the engine.

The objectives are realized by using a combination of empirical and numerical computational fluid dynamics (CFD) simulation techniques. The flow field around the spark gap is calculated and visualized using particle image velocimetry (PIV) technique on a flow bench to study the effect of spark plug geometry on the steady flow across the spark gap. The flow fields resulting from relatively low cross-flow velocities (2.5 m/s and 5 m/s) are studied by means of PIV measurement. CFD simulations are performed for steady cross-flow under ambient conditions to analyze the flow field at high cross-flow velocity conditions. The spark plasma channel response towards the cross-flow velocity is studied using high-speed direct imaging, and attempts are made to correlate the flow with the discharge voltage and current waveforms. The in-cylinder near-spark-plug flow field is estimated using CFD simulations of engine motoring cycles at different intake mass air flow rates. The discharge voltage and current measurements are conducted on a research engine platform during motoring cycles. The spark channel response is compared to the flow field parameters from the simulation data. The overall research methodology is illustrated in Figure 1-7.

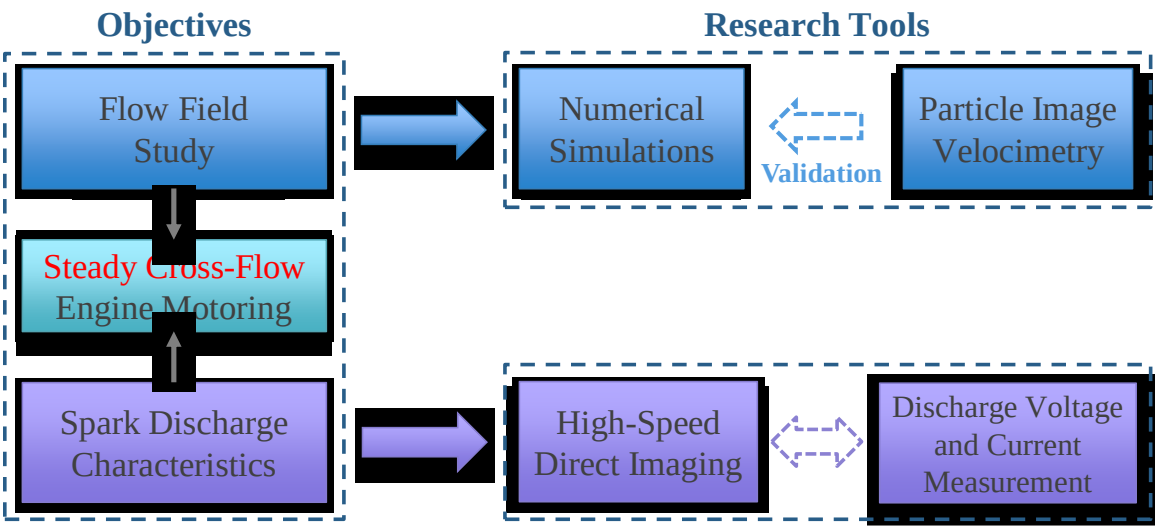

Figure 1-7. Research methodology

1.6 PIV Measurement Technique

Particle image velocimetry (PIV) is a non-intrusive, optical method used to visualize and calculate the instantaneous velocity components of a flow field [36]. This technique uses a laser light sheet as the light source to illuminate the particles in the area or volume of interest, often in a seeded flow. Single or multiple cameras synchronized with the laser pulses and linked to the data acquisition software are used to capture the image data at a relatively high frame rate. The recorded imaging data is then processed using cross/auto-correlation algorithms [36] to obtain the instantaneous flow velocity in the illuminated area or volume.

The non-intrusive nature of PIV measurement helps in analyzing the flow fields without introducing noticeable disturbance to the flow, which is not the case when using physical probe-based methods like hot wire anemometry or differential pressure-based measurement techniques. For instance, PIV is capable of simultaneous measurement of the velocity of the whole flow field across the laser sheet with a resolution as low as 1 mm^2.

The time averaged, as well as the instantaneous, measurements of flow velocity can be obtained [36,37].

The basic principle of PIV measurement is based on the tracking the displacement of small particles in the flow (in the order of a few microns in size) across the image frame sequence to calculate the flow velocity components. The velocity ($\bar{V}$) can be written in terms of particle displacement ($\Delta\bar{X}$) and time interval between successive laser light pulses (Δt) as follows [38],

$$\bar{V} = \frac{\Delta\bar{X}}{\Delta t} \tag{1.1}$$

The particles in the flow are required to be small enough to follow the flow field without altering the flow behavior, and large enough to scatter sufficient light from the laser sheet. Each image of the light sheet is further divided into sub sections called "interrogation windows (IW)" [36]. A minimum particle density of 8-10 particles per interrogation window is required to ensure a strong correlation between image pairs [36]. Corresponding interrogation windows of the image pairs are partially overlapped, and cross-correlated with each other, pixel by pixel. The correlation results in a signal peak where maximum number of particles between both frames match, which detects the average particle displacement ($\Delta\bar{X}$) of all the particles in the interrogation window. Sub-pixel interpolation is then used to calculate the overall displacement and velocity vector for the whole interrogation window. This process is repeated for each interrogation window of the image pair to get the velocity vector map [35]. The cross correlation for PIV is summarized in Figure 1-8 [39].

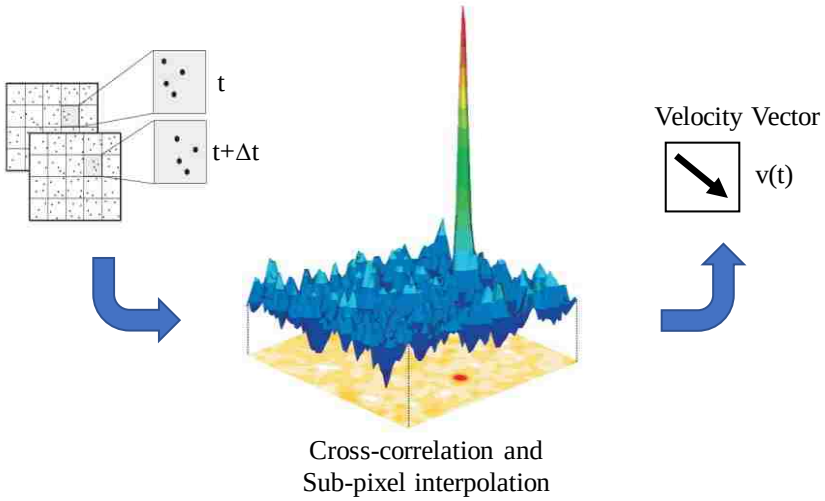

Figure 1-8. PIV cross correlation process (adopted from LaVision [39])

The spatial resolution and measurement range is decided by the interrogation window size and the time between successive laser light pulses (Δt). Interrogation window edge length (d_{IW}) is adjusted to avoid large velocity gradients within a single window.

$$\frac{\frac{S'}{S}.|V_{max}-V_{min}|_{IW}.\Delta t}{d_{IW}} < 5\% \qquad 1.2$$

Where, $\frac{S'}{S}$ is the camera magnification, V_{max} and V_{min} are maximum and minimum particle velocities in a single interrogation window respectively [38].

The maximum measurable flow velocity is constrained by the displacement of particles during the time Δt. The displacement of particles beyond the length d_{IW} results in the loss of correlation between two image frames and hence loss of velocity data. Therefore, the time interval Δt must be small enough to ensure the particle displacement is less than d_{IW}. Typically, taking camera magnification into account, Δt can be estimated using the following equation [38],

$$\frac{\frac{S'}{S}.v.\Delta t}{d_{IW}} < 25\% \qquad 1.3$$

The technique of PIV typically employs a double-pulsed laser module (Nd-YAG) for illuminating the particles in nanosecond interval pulses. Laser pulses are synchronized with the camera to capture each laser pulse. This "frame straddling" allows for the decoupling of measurement velocity and camera exposure, since the maximum illumination time depends on the laser pulse rather than the camera exposure time [40]. For a non-pulsed, continuous laser module, Δt depends on the exposure time of the imaging camera used for data acquisition. Therefore, imaging optics limit the maximum measurable velocity by the PIV system. The difference in particle illumination time interval using pulsed and continuous laser module is shown in Figure 1-9.

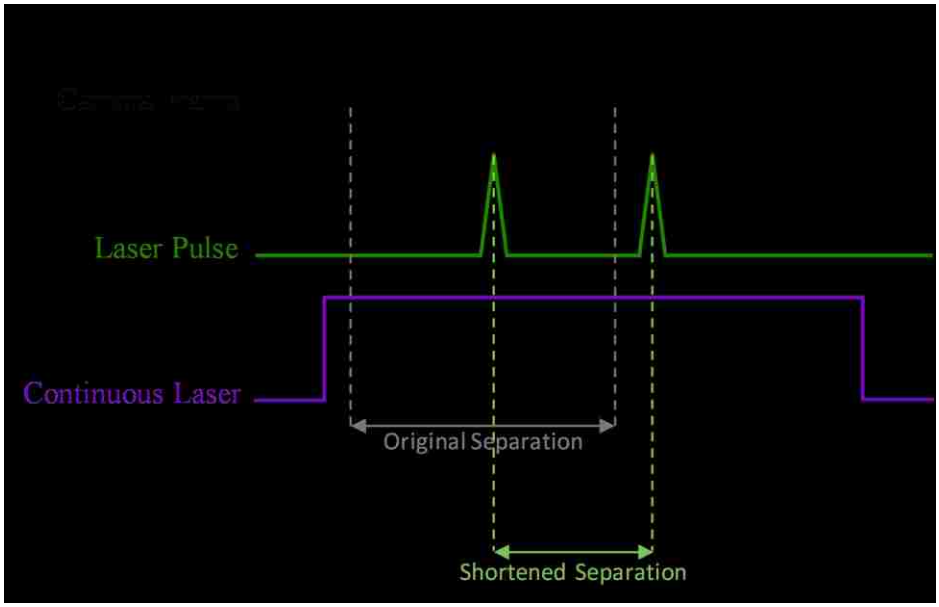

Figure 1-9. Frame straddling using pulsed laser

1.7 Structure of the Thesis

The thesis consists of six chapters. It is divided into four sections. First section, consisting of Chapter 1 and Chapter 2, provides the research motivation, background, associated challenges, and a review of past literature relevant to the author's research. The main objectives of this research are outlined in chapter 1. The PIV measurement technique is also introduced in this chapter. Chapter 2 provides a detailed literature review previous researches on the spark plasma behavior under flow conditions.

Details of different tools and methodologies used in this research are discussed in the second section, which consists of Chapter 3. The schematics and specifics of the high-speed direct imaging setup, the discharge voltage and current measurement circuit, the steady flow PIV measurement system, the engine test platform and the CFD simulation parameters are provided.

The third section consists of Chapter 4 and Chapter 5. The findings from the numerical simulations and the empirical data are discussed in this section. The results from the steady cross-flow investigation are presented in Chapter 4. The effect of spark plug geometry on steady cross flow is examined using numerical simulations and PIV measurements. The spark channel response to a steady cross-flow is studied using high-speed direct imaging and discharge voltage and current measurements. Engine testing results are discussed in Chapter 5. Efforts are made to correlate the near-spark-plug flow velocity from numerical simulation and spark restrikes from discharge voltage measurements.

The fourth section provides the summary of the research outcomes, conclusions and recommendations of future work in Chapter 6. Further information regarding references, appendices and a list of publications is provided at the end.

LITERATURE REVIEW

A detailed review of literatures relevant to author's work is presented in this chapter. A study of previously published work on the effect of local flow field on the spark discharge characteristics and the use of this electrical discharge to estimate the variations in the in-cylinder flow velocity, also known as spark anemometry, is presented in this review.

2.1 Effect of Spark Plug Geometry on Local Flow Field

The in-cylinder charge motion is an effective way to increase the combustion efficiency and shorten the combustion duration of lean mixtures in SI engines [21-23]. Large scale eddies created during the charge induction often break up into small scale turbulence during the compression stroke. The flow field near the spark gap can be influenced by the bluff body effect of the spark electrodes [26,41]. Therefore, the background conditions for the flame kernel formation can be determined by the overall in-cylinder flow field including the local disturbances caused by the spark plug.

Halldin studied the effect of spark electrodes on the flow velocity and turbulence using laser doppler velocimetry (LDV) measurements near the spark gap under steady flow at ambient pressure and temperature [26]. He also investigated the effect of spark electrode orientation with respect to mean flow at three different turbulence levels. His findings demonstrated that the spark plug geometry had a substantial effect on the local flow field. The flow velocity in the spark gap remained higher than the mean flow velocity for all turbulence levels. The turbulent intensity shows an opposite trend with the lowest value across the spark gap as compared to the surroundings. The position of the ground electrode relative to the mean flow direction was of great significance for the velocity field near the

spark gap. Velocity gradients near the two electrodes were very small, indicating a very thin boundary layer on the electrode surface.

It has been reported in the literature that the turbulent flow near the spark gap can aid in ignition by enhancing the flame kernel propagation speed and providing the fresh charge to the spark channel [32,42-44].

2.2 Effect of Flow Field on Spark Ignition

The local flow field can have a significant effect on the spark discharge process. Introductions to the spark breakdown and the flow effect on the glow phase have been provided in section 1.4. There has been a considerable amount of research done on the effect of flow on the spark ignition and subsequent combustion on various engines as well as on various constant volume combustion vessel platforms [27-30,45-50]. An overview of the effect of flow on different aspects of spark discharge and flame initiation is presented in this section.

Sayama et al. investigated the spark discharge and early flame kernel propagation at lean-burn conditions with air-fuel ratios of 20:1 – 30:1 under a relatively high flow velocity of 65 m/s in an optically accessible constant volume combustion chamber designed to impart rotational motion to the air-fuel mixture to simulate the engine-like conditions [29,30]. The authors found that the spark channel, under the effect of flow field, stretched to follow the flow. Frequent short circuits and restrikes were observed. These short circuits and restrikes were dependent on flow velocity and ignition energy supplied to the spark. Additionally, the time before the first restrike after the spark breakdown was longer for the high ignition energy case as compared to the lower ignition energy. Similar trend was observed for the

spark stretch length. Their findings also demonstrated that the degree of dilution had a significant effect on subsequent flame development after the initial spark event.

Arcoumanis and Bae used shadowgraph imaging to study the effect of orientation of spark plug with respect to the mean flow direction in a cylindrical combustion chamber [45]. They concluded that the actual flow field in the spark gap was influenced by the protruding electrodes. The flame kernel development and propagation were more dependent on the orientation of the ground electrode at higher flow velocity and turbulence intensity. For the orientation with the ground electrode positioned upstream of the spark gap, the flame development was relatively slower because of the reduced local flow velocity within the spark gap as a result of the shrouding effect of the ground electrode.

Dulger et al. investigated the effect of different parameters including spark current, orientation, electrode gap, and flow velocity on the lean misfire limit of spark ignition of butane-air mixtures under flow conditions [46,47]. The results revealed that under moderate gap flow velocities (7-9 m/s), the cross-flow orientation was found to be the most effective in extending the lean limit. At lower flow rates, the upstream ground electrode placement was marginally better than the downstream ground electrode.

Ballal and Lefebvre studied the different spark discharge variables in flowing propane-air mixture under different velocities (up to 100 m/s), pressures and flow turbulence (1% to 15%), in a small wind tunnel [48]. The variables included the breakdown voltage, the spark duration and energy. Their results showed that the minimum ignition energy of the mixture increased with the cross-flow velocity but was relatively unaffected by the small scale turbulence. If all other conditions are kept constant, this implies that the energy utilized for

ignition during spark discharge increased slightly with increase in velocity. Spark discharge response to cross-flow velocity is very consistent and reproducible.

Experiments were performed by Clean Combustion Engine Lab (CCEL) research group at University of Windsor on spark discharge under cross-flow conditions, in constant volume chamber. The results indicated that the spark gap resistance and discharge voltage increased with higher flow velocities [27,28]. The restrike behavior similar to the one seen by Sayama et al. [29,30] was observed. Using the TCI system, the discharge energy increased by 10-20% and the overall spark duration reduced by 50-60%. The discharge energy increased linearly with higher flow velocity up to 25 m/s, beyond which the energy level tends to remain the same. The boosting of the discharge current level helped in maintaining the discharge plasma stretch for a longer duration under flow conditions.

Johansson examined the effect of several important parameters including the local flow field, mixture composition, and temperatures on the cyclic variability of early combustion processes [49]. He concluded that cyclic variations in flow field turbulence and local mixture composition had a significant impact on the fluctuations in spark ignition and early flame growth.

Schild investigated the effects of flow velocity (30m/s to 140m/s) on spark ignition in a pulsed detonation engine at different ignition energy levels (250mJ to 4J) using high speed schlieren imaging [33]. He found that at lower ignition energy, the flow velocity initially promoted the flame propagation. However, as the flame stretch increased, the flame with high flow velocity was partially extinguished and was unable to sustain the flame propagation. The flame speed after the initial flame kernel formation was similar for the

two highest flow velocities tested (90 m/s and 140 m/s). It was possible to overcome the high velocity and resulting turbulence effects by increasing the ignition energy.

2.3 Spark Anemometry

The use of the spark discharge response as an estimator for flow velocity was first reported in 1932 by Lindvall [51]. Since then various researches have tried to further develop this technique as an indicator of cyclic variations in velocity during the engine operation, which offers a relatively simple way of obtaining approximate velocity measurement [41,51-55]. Some of the literature published on the use of spark anemometry (use of electrical discharge to estimate flow velocity) has been discussed in this section.

Kim et al. used spark anemometry to estimate the in-cylinder flow velocity near the spark plug in three different production engines, under low load operation (2.6 bar BMEP at 1500 rpm) [41]. The authors used hot wire anemometer to measure the flow velocity near the spark gap under ambient conditions and recorded the voltage waveforms corresponding to different flow velocities. A data driven model developed from the measurement data was used to predict the bulk flow velocity near the spark plug in the engine using the discharge voltage profiles. The predicted flow velocity produced tangible correlations with the measurements from fiber optics equipped spark plug.

Gardiner et al. studied the use of spark anemometry based on the data from steady flow tests at ambient conditions. They used a data driven model with approximate corrections for the pressure change during engine operation, to estimate the gap flow velocity inside a firing engine [55]. The authors used constant discharge current profile instead of the typical TCI decaying current. Due to lack of optical access or other means to verify the estimated velocity, only qualitative comparison about the velocity trends could be made.

RESEARCH TOOLS

The research tools and methodologies used in this study are described in this chapter. Details including, schematic diagrams, measurement devices and circuit diagrams, where applicable, are provided for various research platforms. The empirical research tools include the steady flow PIV setup, spark channel imaging, discharge voltage and current measurements, and the engine research platform. Additionally, the CFD simulation parameters for steady cross-flow and engine motoring cases are discussed.

3.1 Steady flow Particle Image Velocimetry (PIV)

The flow field visualization and velocity measurement tests are conducted on an in-house designed flow bench using PIV optical technique. The steady flow bench was previously designed and fabricated in the author's lab to measure the swirl generated by the intake port of engine cylinder head [21]. For this research, the cylinder head section of the flow bench is replaced with a rectangular flow channel containing an M14 conventional J-type spark plug. The schematic drawing of the flow bench including the flow channel with spark plug is shown in Figure 3-1. The air flow through the flow channel is generated by the "air box" containing four independently controlled commercially available blower motors (Ametek Lamb 115923). Selective air flow rates can be generated by activating the corresponding number of motors. Finer adjustments to the flow rate can be made by controlling the electrical throttle body opening upstream of the air box in addition to a bleeding valve mounted downstream of the air box. The flow rate of the air is measured by a sharp-edge orifice flow meter, which is manufactured according to ISO 5167-1:2003 standards [56]. Geometric dimensions of the orifice meter are outlined in Table 3-1.

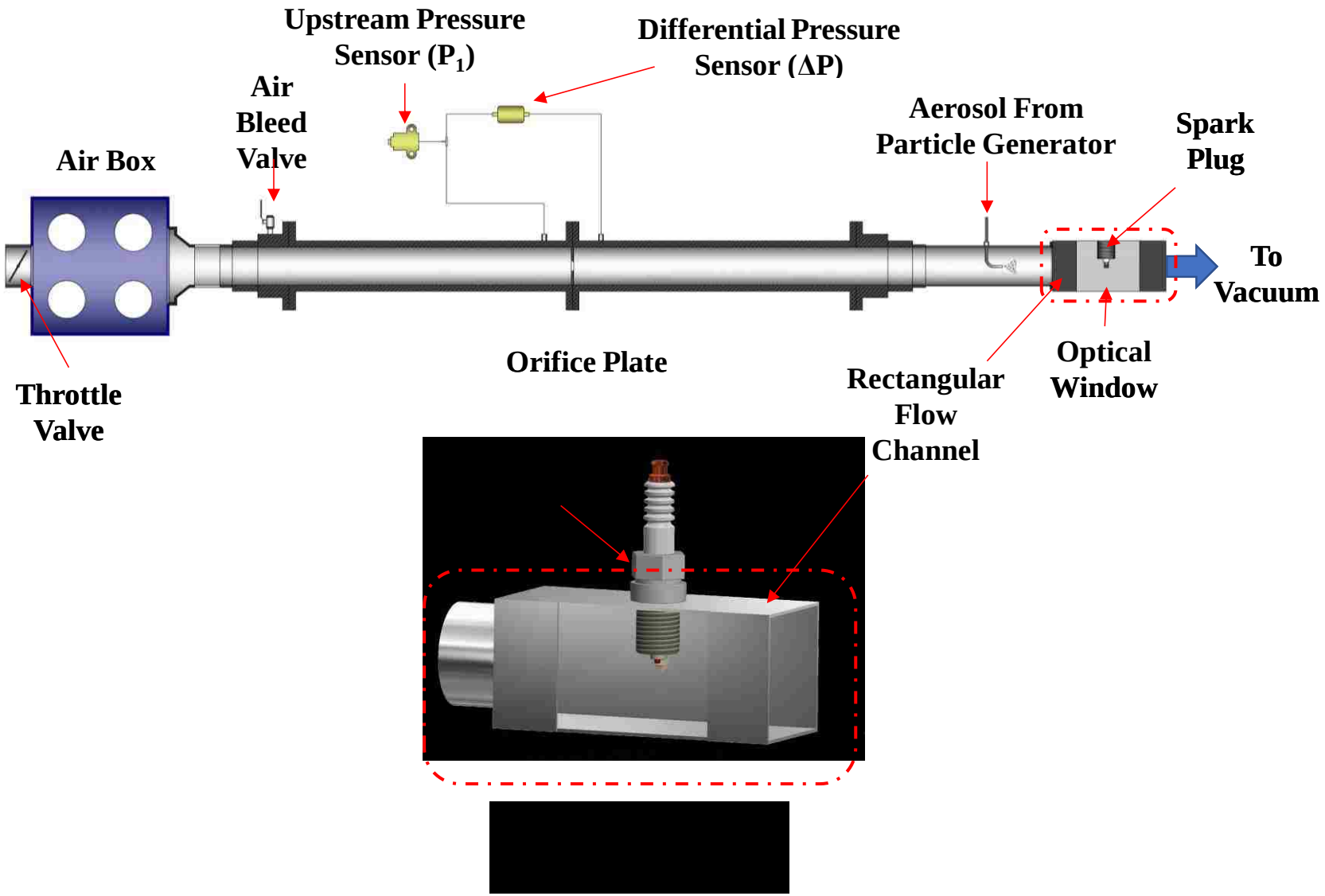
Upstream Pressure Sensor (P_1)
Differential Pressure Sensor (ΔP)
Air Bleed Valve
Air Box
Aerosol From Particle Generator
Spark Plug
To Vacuum
Throttle Valve
Orifice Plate
Rectangular Flow Channel
Optical Window

Table 3-1. Sharp edge orifice meter dimensions

Dimension	**Value**
Orifice diameter	33 mm
Pipe internal diameter	55.8 mm
Pipe upstream length	781.2 mm
Pipe downstream length	390.6 mm
Pressure tapping – distance upstream from orifice	55.8 mm
Pressure tapping – distance downstream from orifice	27.9 mm

The pressure difference across the orifice flow meter is measured using an NXP USA MXPV7025 digital differential pressure sensor [21] and the pressure upstream of the orifice meter is measured using an Ametek SPT0100X140 (0-100 psi) pressure transducer [21]. The upstream pressure and the pressure difference across the orifice plate are used to calculate the mass flow rate of the incoming air. The measured flow rate is then used to help calculate the flow velocity upstream of the spark plug. The calculated flow velocity is used as reference during the experiment. The conventional J-type spark plug used for the study has a central electrode of diameter 2.6 mm and the spark gap is 0.9 mm.

The air flow downstream of the orifice flow meter is seeded with the tracking particles before it enters into the rectangular flow channel. In this research, olive oil aerosol is used as tracer for the flow visualization and velocity measurements. The aerosol particles are generated using an in-house fabricated variation of laskin nozzle atomizer. This is a twin-fluid atomizer where pressurized air is used as the atomizing media [57-59]. The laskin nozzle design is presented in Figure 3-2. High speed air jets are created in the atomizer fluid (olive oil) by small holes in the nozzle tube. The nozzle tube consists of a 10 mm

inner diameter aluminum tube with four holes, each with 1.5 mm diameter, drilled at 0º, 90º, 180º and 270º, approximately 25 mm from the base of the tube (Figure 3-2). The tube base is then plugged by welding to a small aluminum cap at the end.

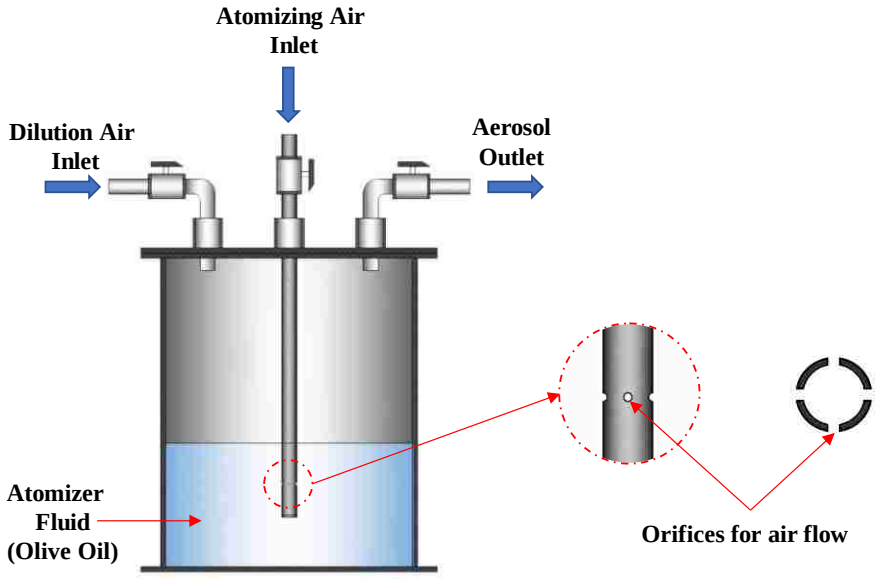

Figure 3-2. Seeding particle generator schematic

The droplet size distribution depends mainly on the liquid used and is only slightly dependent on the feed air pressure [60]. Oils tend to generate smaller size droplet than water. Additionally, water has lower boiling point compared to oils, which can lead to water droplets evaporating on the laser light sheet. This results in relatively uneven particle density as compared to oil droplets.

The number of particles can be controlled by changing the feed air pressure, higher pressure leads to a higher particle density in the resulting aerosol. Alternatively, additional nozzles can be added to the same atomizing air supply to increase the number of particles. The particle density can also be reduced and homogenized by supplying the dilution air. A desired output concentration can be achieved by adjusting the dilution and feed air pressure/number of active nozzles.

For the present study, 3 bar atomizing air pressure through a single nozzle, with no dilution air is used to generate the olive oil aerosol. Particles are introduced into the main flow, upstream of the rectangular flow channel to facilitate proper mixing for generating a uniform flow seeding pattern for PIV.

The light sheet generated by a 2W, 450 nm (blue) continuous laser module is used to illuminate the particles in the flow. The sheet generation optics include a plano-concave cylindrical lens followed by a plano-convex cylindrical lens. The plano-concave cylindrical lens with 12.5 mm focal length is used to convert the incoming laser beam into a light sheet and the thickness of the sheet is controlled by the plano-convex lens with a longer, 50 mm focal length. The flow channel with the optical setup is presented in Figure 3.3.

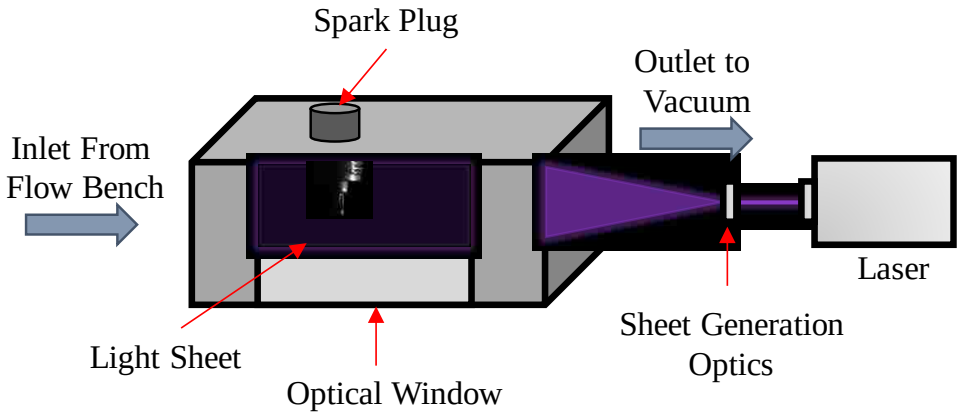

Figure 3-3. Optical Setup for PIV

The image data is captured in greyscale using a Phantom Vision Research v7.3 high speed complementary metal-oxide semiconductor (CMOS) camera. The camera has a full-scale resolution of 800×600 pixels. It is capable of sampling the image data at 6,688 frames per second (fps) at full resolution and up to 190,000 fps at 32×32 pixels resolution at a user defined exposure time. The sampling rate of 10,000 fps at 512×256 pixels resolution with

an exposure duration of 90 μs is used to capture the image data for this PIV analysis. The spark plug and the internal surface of the flow channel is painted black to minimize the reflections from the laser sheet.

Since a continuous laser module is used as light source instead of pulsed laser module, the illumination time of the tracer particles on an image frame is controlled exclusively by the exposure time of the camera. At the upper end, exposure time is restricted by the sampling rate of the camera. The maximum exposure limit corresponds to the time between two successive image frames. At the lower end, the exposure time is limited by the amount of light (scattered by the particles in the flow) detected by the camera sensor. The smallest exposure time that can capture the scattered light from all the particles illuminated by the laser light sheet is the minimum exposure limit. Reducing the exposure time beyond the minimum exposure limit results in data loss i.e. a reduction in number of detected particles. This can lead to weaker correlation between image pairs, which increases the measurement uncertainty.

The minimum exposure limit confines the flow velocity to be measured by PIV, for this experimental setup, in a narrow range. With the increase in the flow velocity, the continuously illuminated particles appear as ‘streaks’ (lines) instead of single particles. This behavior is evident from Figure 3-4, which shows the raw image frames at two different flow velocities. Particles with the flow velocity 6.8 m/s (Figure 3-4 (b)) already appear to be transitioning into streaks. To keep the measurement uncertainty in check, the maximum cross-flow velocity is limited to 5 m/s.

The image data acquired from PIV measurement tests is post-processed using an open source MATLAB code called PIVLab. The code solves the cross correlation and makes

the sub pixel estimations between image pairs, according to user input values of interrogation window size, to generates the velocity vector map of the flow field [61].

(a)

Flow Velocity = 3 m/s Exposure = 90 μs

(b)

Flow Velocity = 6.8 m/s Exposure = 90 μs

Figure 3-4. Raw PIV image frames at different flow velocities: (a) 3 m/s and (b) 6.8 m/s

The PIV image data is processed using a MATLAB code PIVLab in three steps. First, the image is pre-processed to increase the contrast in order to make particle identification easier. Then, the image pair cross correlation is solved using a relatively large interrogation window size of 64×64 pixels (px) and a step size of 32 px. Finally, the window size is decreased to 32×32 px and the corresponding step size is reduced to 16px to increase the measurement resolution. The chosen step size resulted in a 50% overlap. Fast fourier transformation (FFT) window deformation algorithm is used for solving the correlation in order to decrease the total solution time [61]. A median filter is applied to remove the spurious vectors that have locally large standard deviations. An image mask is drawn onto the raw images to exclude the areas with no laser illumination from the correlation process.

Figure 3.5 shows the image mask and the size of the interrogation window used for the analysis. The areas in red color are excluded from the final analysis.

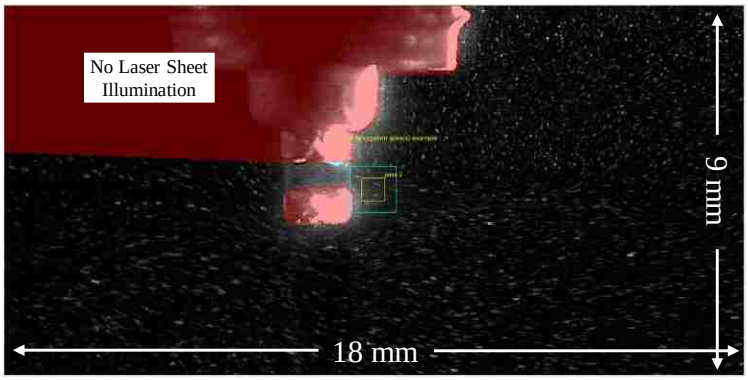

Figure 3-5. PIV Image analysis in PIVLab

3.2 Spark Discharge Characteristics Measurement

A combination of high-speed direct imaging of spark channel, and electrical parameters (voltage and current profile) measurements are used to record the spark discharge characteristics under quiescent as well as steady cross-flow at ambient pressure and temperature. Conventional Transistor Coil Ignition (TCI) system is used for the discharge characteristics study. Details of the measurement system are presented in Figure 3-6.

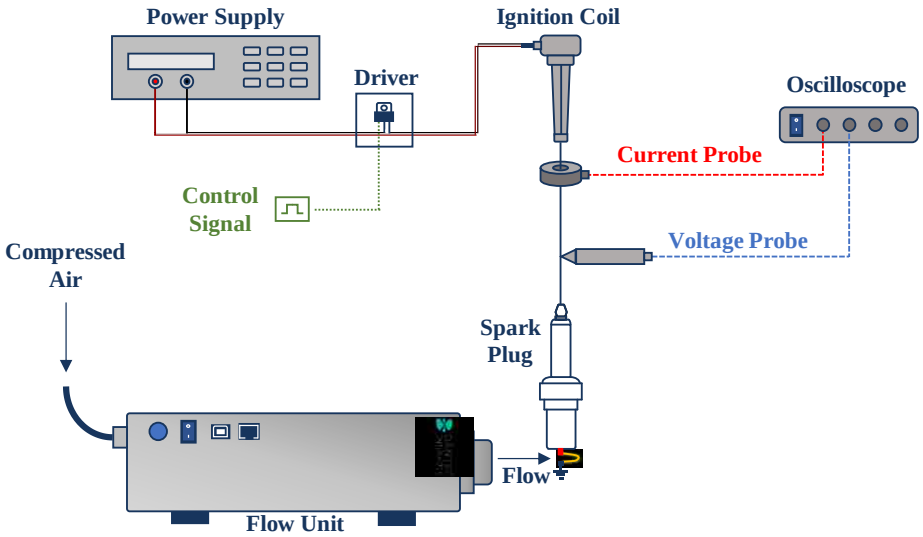

Figure 3-6. Spark discharge characteristics measurement system

The steady flow across the spark gap is generated with a Dantec Dynamics 90H02 Streamline Flow Unit. The flow unit is capable of generating steady flow over a wide velocity range of 0.2 m/s to 300 m/s. Tests are conducted under the cross-flow velocities between 5 m/s and 50 m/s. The charging process of the ignition coil is controlled by an insulated gate bipolar transistor (IGBT, V3040p). A National Instruments real time (RT) controller with a field programmable gate array (FPGA) module is programmed to generate the control signal to the IGBT for an ignition coil charging duration of 2 ms. The discharge voltage is measured by a Tektronix P6015 high voltage probe. The P6015 is a ground-referenced 100 MΩ, 3 pF high voltage probe with 1000X attenuation. A Pearson 411 toroid shaped current probe is used for the discharge current measurement. The measurement data is recorded by a high-precision digital oscilloscope (PicoScope 4824). The circuit of ignition system with the locations of measurement probes is shown in Figure 3-7.

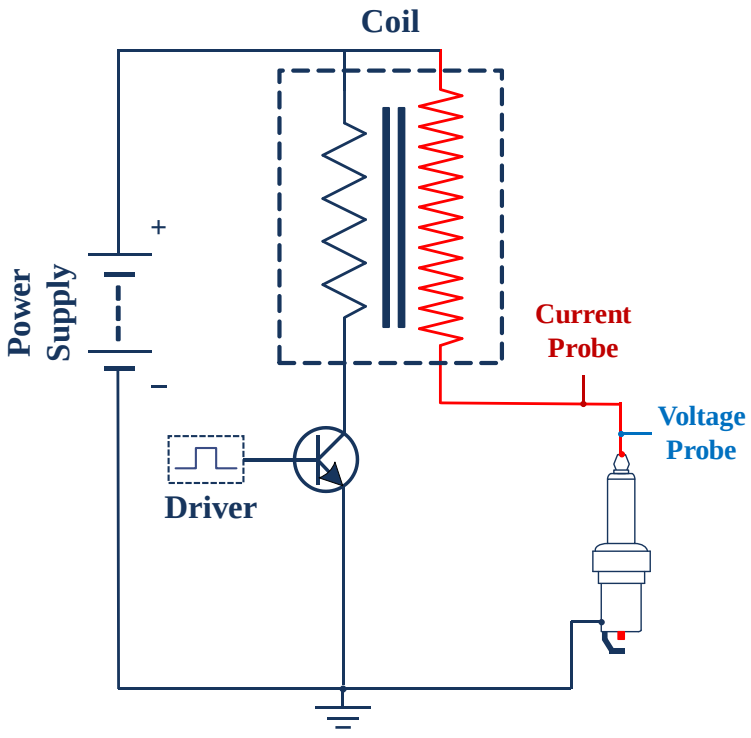

Figure 3-7. TCI system circuit diagram with probe locations

Direct images of spark plasma channel are taken using a Phantom V7.3 high speed camera. An exposure duration of 14 μs at a resolution of 256×128 pixels is used for recording the direct imaging data at a sampling rate of 65,400 fps.

3.3 Engine Test Platform

The test engine platform used in this research is a Yanmar NFD-170, a two-valve, four stroke, single cylinder diesel engine. The engine is extensively modified for the spark ignition research. The modifications include reducing the compression ratio to 9.2:1 by modifying the piston geometry, replacing the diesel injector with a spark ignition system, and installing a port-fuel injection system. The piston bowl shape is altered to match that of a typical spark ignition engine. Major geometrical specifications of the engine are summarized in Table 3-2.

Table 3-2. Test engine specifications

Engine type	Yanmar NFD-170, 4-stroke, 2-valve SI
Bore	102 mm
Stroke	105 mm
Connecting rod length	165 mm
Displacement	857 cm^3
Compression ratio	9.2:1
Speed	1300 rpm

The engine is connected to a 40 horsepower General Electric® 26G215 direct current (DC) dynamometer for speed control and torque measurements, which is operated through a Dyne Systems Dyn-Loc IV digital dynamometer controller. The intake pressure is

controlled through an electronic pressure regulator. The intake air flow rate is measured using a ROOTS volumetric flow meter (5M175) mounted before the intake surge tank. All motoring tests are performed at the naturally aspirated conditions. A helical insert is installed upstream of the intake port to increase the port generated swirl into the engine [21]. The spark plug used for ignition and spark anemometry is a conventional J-type resistive spark plug with 14mm metric thread. The discharge voltage and current are measured by a Tektronix P6015 high voltage probe and a Pearson 411 current probe respectively and the measurement data is recorded using a Picoscope 4425 oscilloscope. The in-cylinder pressure is recorded using a Kistler piezo-electric pressure transducer (model 6043A60), coupled with a Kistler 5010B charge amplifier. The pressure data is synchronized with the crank position using a crankshaft rotary encoder (Gurley Precision Instruments) and a camshaft sensor. The manifold pressure is measured using a Kistler piezo-resistive type absolute pressure transducer (model 4075A10). The National Instruments - data acquisition (NI-DAQ) card along with the LabVIEW 2010 software package is used to record the pressure data at a 0.1 crank angle degree (° CA) resolution. A liquid cooling system (FEV Coolant Conditioning Unit) is used to maintain the engine coolant temperature at 80 °C. This engine research platform is instrumented for a detailed emission measurement. The schematic diagram of the engine test platform showing relevant details is presented in Figure 3-8. The spark discharge voltage and current profiles are recorded during the ignition window of 305° to 355° CA with a 10° CA increment during engine motoring at 1300 rpm. The mass flow rates of 3.53, 4.85 and 5.56 g/s are used for the engine tests.

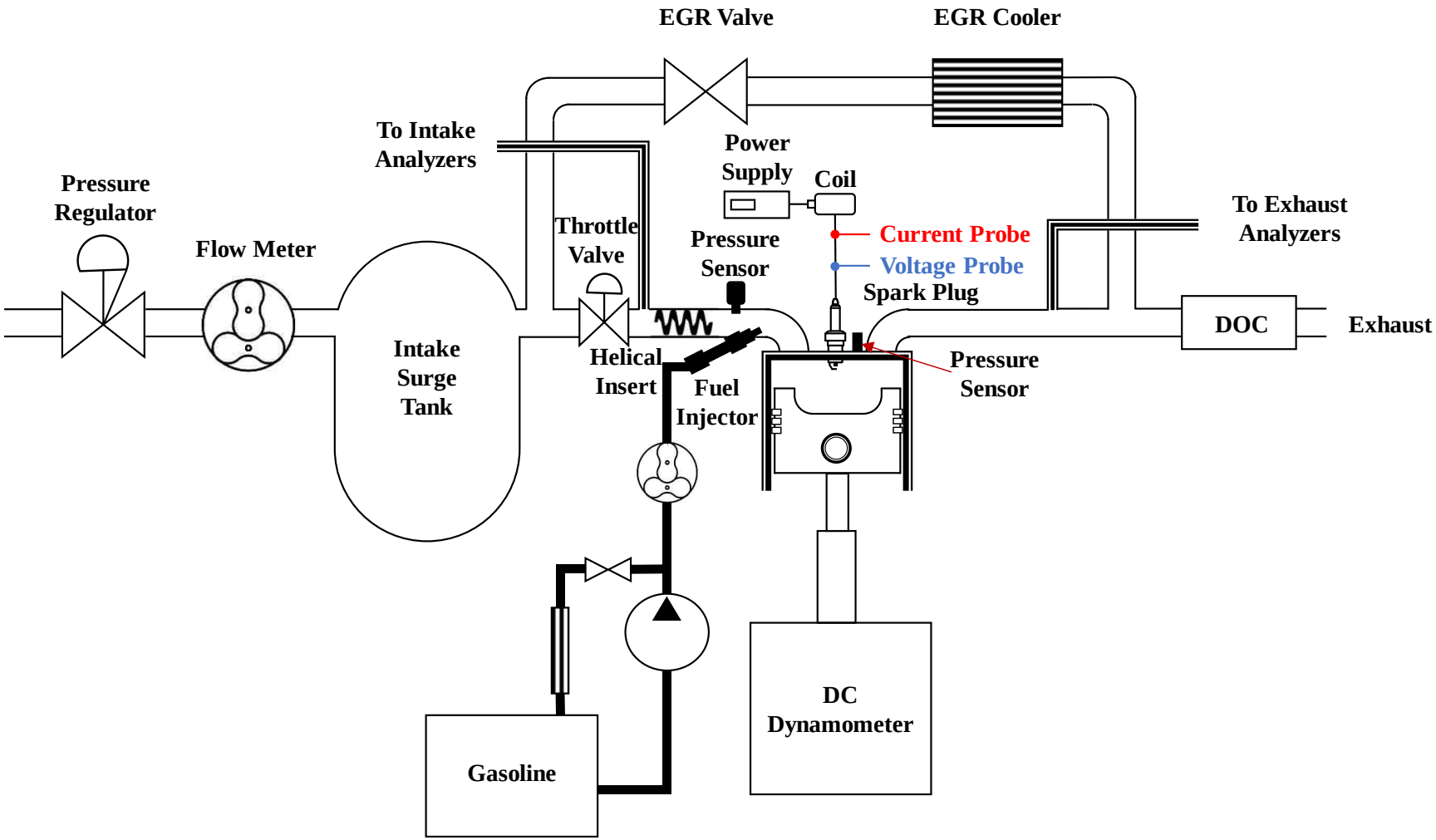

Figure 3-8. Engine test platform

3.4 Numerical Simulation

The three-dimensional CFD simulations are performed to estimate the flow field around a conventional J-type spark plug. Two types of flow fields are simulated, a steady cross-flow under ambient conditions, and the flow field near the spark gap during the ignition window under engine motoring conditions. As described earlier, the PIV flow field study is restricted to a relatively low cross-flow velocity of 5 m/s due to the limitations of the experimental setup. A numerical simulation study is undertaken to supplement the experimental results and analyze the flow field at higher velocity conditions. The PIV measurements are used to validate the steady cross-flow numerical model results. The flow turbulence is analyzed in terms of turbulent velocity and vorticity magnitudes. For the engine simulations, the flow field in the vicinity of the spark plug is simulated at different intake mass air flows. The results are then compared to the spark plasma response using discharge parameters measurements. Due to the non-availability of an optical access into the engine, there is no direct validation of the simulated flow results. The gas exchange process is validated using the in-cylinder pressure measurements. Simulation parameters for both cases are described in following sub-sections along with geometrical and numerical models.

3.4.1 Steady Cross-Flow

The numerical simulations are performed using Converge^{TM} CFD simulation suit version 2.3. The software uses an automatic grid generation algorithm with user defined grid embedding as well as adaptive mesh refinement (AMR) to enhance the accuracy and resolution of the simulation results. The numerical results are post-processed using ANSYS Ensight 10.1 software.

The geometry of the spark plug with key dimensions is presented in Figure 3-9. The diameter of central electrode of the spark plug is 2.6 mm and the distance between the central and the ground electrode, termed as spark gap, is 0.9 mm.

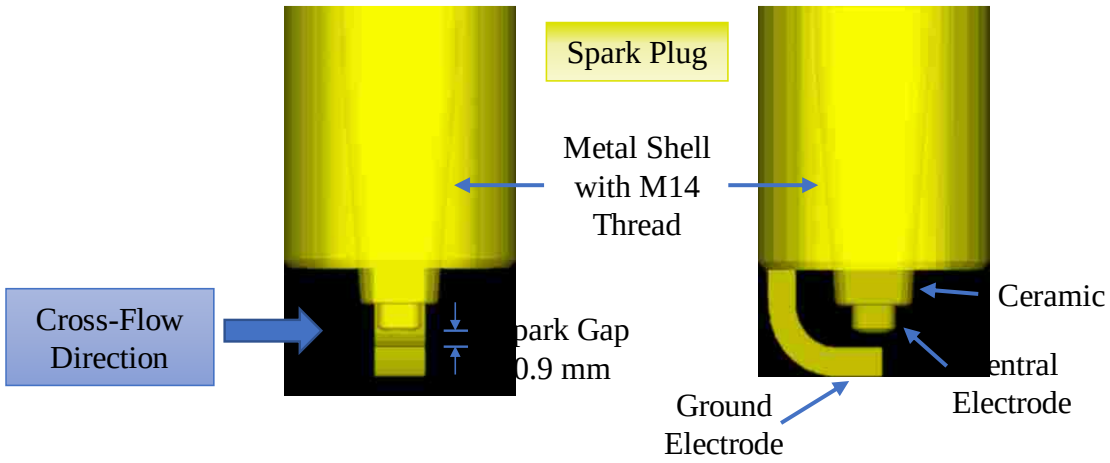

Figure 3-9. Geometrical model of conventional J-type spark plug

The final model of the computational domain is shown in Figure 3-10. The model includes the spark plug enclosed in the flow channel, with the dimensions similar to the experimental setup. The enclosure and the spark plug surfaces are modelled as "law of wall" wall boundaries to enable the boundary layer generation and to resolve the viscous sub-layer in turbulent flows by reducing the velocity next to fluid-solid contact surface to zero [62]. A steady cross-flow is maintained through a constant inlet velocity boundary condition. The inlet velocity is varied form 2.5 m/s to 100 m/s. Lower flow velocity cases (2.5 m/s and 5.0 m/s) are used for model validation using the PIV flow field results. A steady pressure-based solver is used for all velocities below 100 m/s, thereafter for the 100 m/s inflow velocity case, density-based steady solver is used since this solver is recommended for flow simulations that experience Mach numbers greater than 0.3 [62]. For the flow with Mach number less than 0.3, the pressure-based solver is more efficient

than the density-based solver [62]. The wall temperature and initial pressure are set to 300 K and 1 bar respectively.

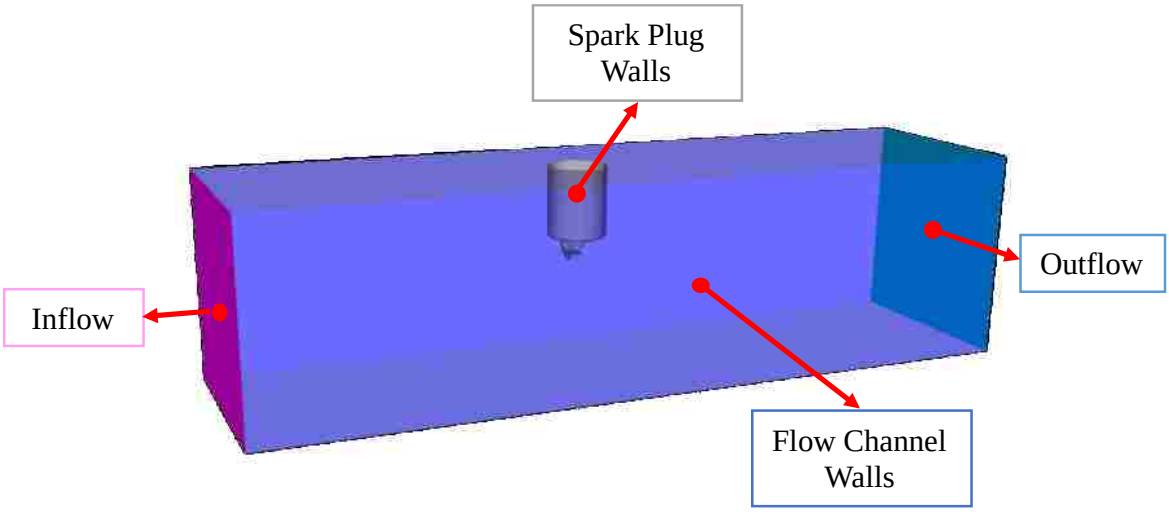

Figure 3-10. Computational model for steady flow simulation

The grid size refers to the edge length of the cube shaped mesh cells. The base grid size for the simulation is 4 mm to decrease the total computational load. After 2500 seconds of simulation time, a fourth level refinement is used in a cylindrical section in the vicinity of the spark gap, reducing the local grid size to 0.25 mm to increase the resolution of velocity and other flow parameters. The position and profile of grid refinement are shown in Figure 3-11. The total solution time of 5500 seconds is required for the flow to reach a steady state, which is evident by the convergence of flow parameters.

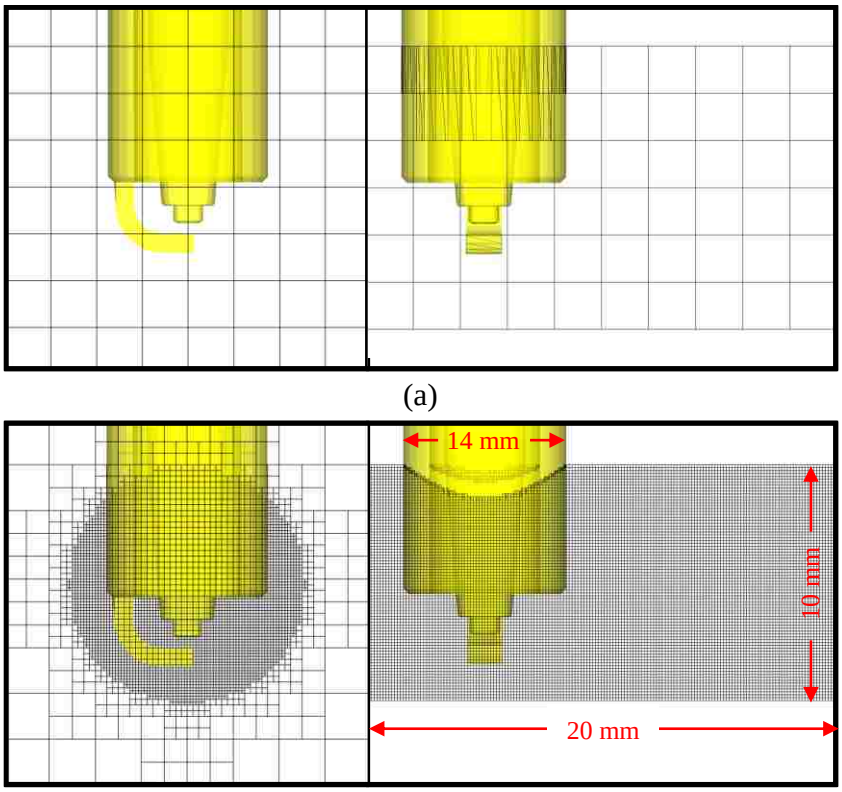

Figure 3-11. Grid refinement for the simulation: (a) No grid refinement before 2500 s, (b) Cylindrical grid refinement region in the vicinity of the spark gap

The standard k-ε model is used to simulate turbulence parameters. This model is a two-equation model that solves for the turbulent kinetic energy k and the turbulent dissipation ε [62]. Major simulation parameters for the steady cross-flow case are summarized in Table 3-3.

Table 3-3. Converge simulation parameters for steady cross-flow

Parameter	**Value**
Intake velocity	2.5/5/10/20/30/40/50/100 m/s
Intake temperature and pressure	300 K, 1 bar
Grid size (edge length)	4 mm (max) / 0.25 mm (min)
Turbulence model	Standard k-ε model

3.4.2 In-Cylinder Near-Spark-Plug Flow Field

The engine geometry is carefully modeled to match the research engine platform used for engine tests. The insert used in the intake manifold and the helical port are incorporated into the geometry input. Since the overall in-cylinder is influenced significantly by the intake port design, laser scan of a flexible foam mold of the helical intake port is used to create the surface file, which is used in overall engine geometrical model [21]. The computational domain with major boundaries is presented in Figure 3-12. The intake mass air flow rates of 3.53, 4.85 and 5.56 g/s are simulated. The simulation study is mainly focused on the spark event and early flame development period. Thus, to save the computational time, a part of a single motoring cycle, which includes the intake, compression and expansion strokes are simulated. The intake manifold pressure data, recorded at a 0.1° CA resolution during the engine motoring tests, is used as inflow boundary condition for the intake port upstream of the insert. The intake and exhaust valve profiles were measured in author's lab using the dial indicator [21].

A base grid size of 4 mm with a time varying grid refinement is used. During the charge induction process, when intake valve is open, the grid size near the valve is set to 1 mm. The grid size in the cylinder region is refined to 1 mm during the intake and expansion strokes. It is further refined to 0.5 mm during the spark event and in the ignition window of 290° to 370° CA. During this period, the grid size near the spark gap is reduced to 0.25 mm to increase the resolution of the flow field. The grid size distribution near the spark gap during the spark event window is shown in Figure 3-13. This final grid size is selected based on the incremental refinements until the computational power required to achieve a significant improvement becomes unfavorable.

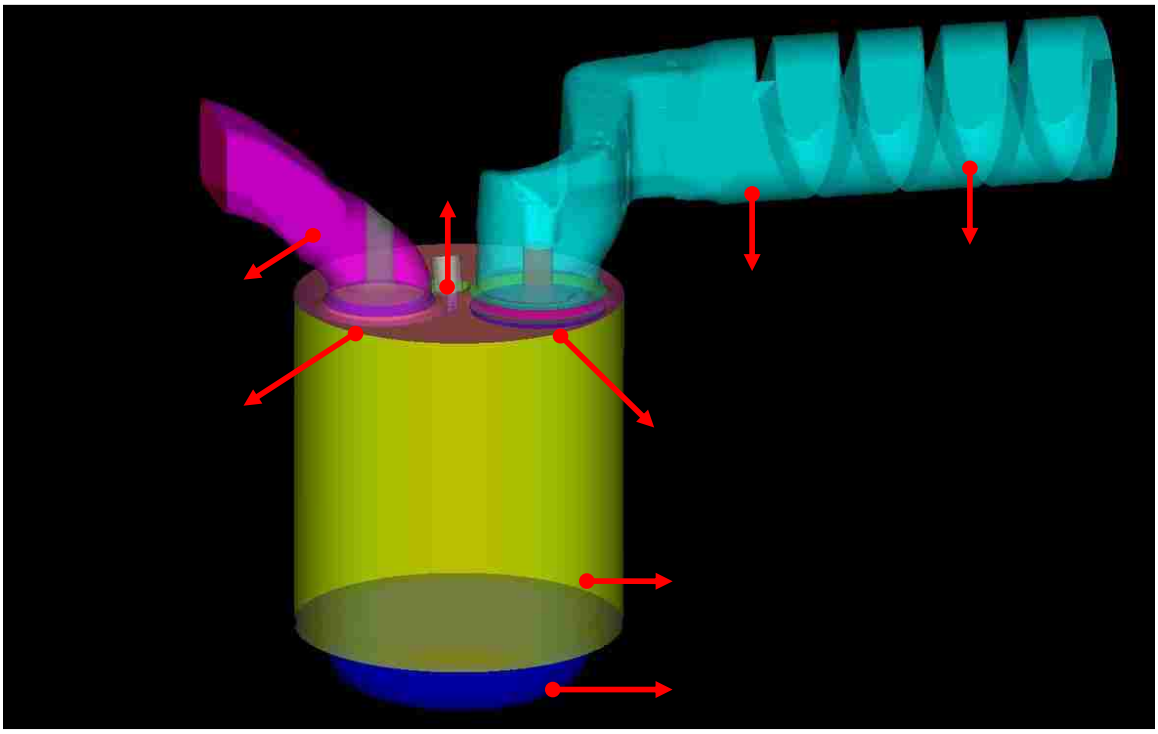

Figure 3-12. Computational model for engine motoring simulations

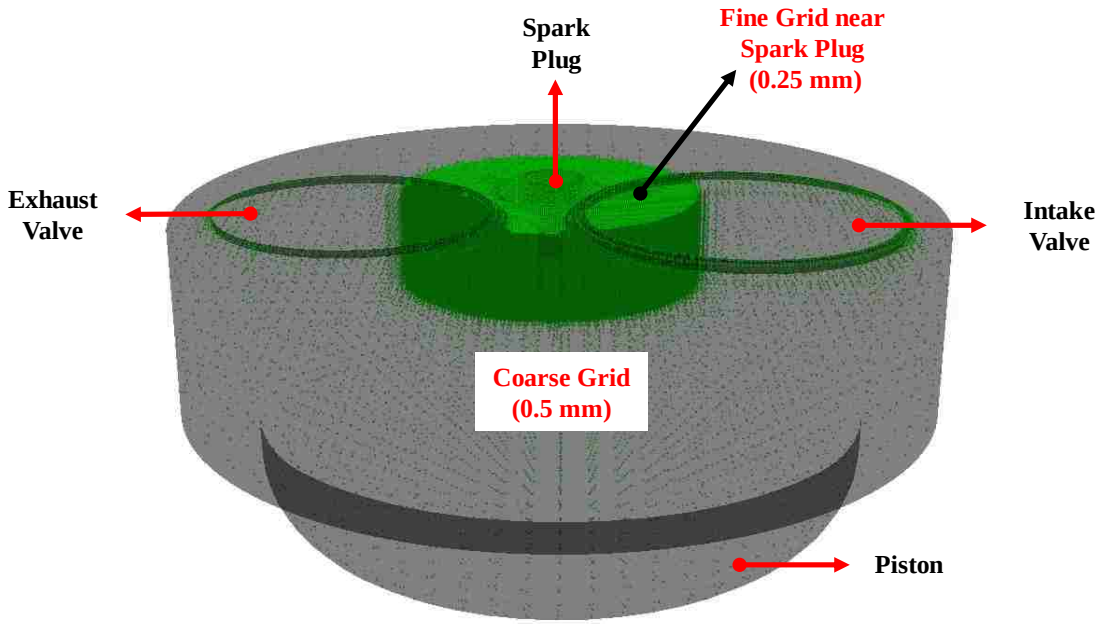

Figure 3-13. Grid refinement during engine motoring simulations at 310° CA

Turbulence is resolved using the renormalized group (RNG) k-ε turbulence model. The RNG k-ε model is a variation of the standard k-ε turbulence model. It includes additional terms which improves the accuracy for the rapidly strained and swirling flows [62]. Major simulation parameters for the in-cylinder flow simulation are summarized in Table 3-4.

Table 3-4. In-cylinder flow simulation parameters

Parameter	**Value**
Intake temperature	300 K
Intake pressure profile	Manifold pressure from empirical data
Intake mass flow rates	3.56/4.85/5.56 g/s
Cylinder wall temperature	353 K
Grid size (edge length)	4 mm (max) / 0.25 mm (min)
Turbulence model	Standard k-ε model
Engine Geometry	Yanmar NFD-170
Bore	102 mm
Stroke	105 mm
Engine Speed	1300 rpm
Compression Ratio	9.2:1
Intake valve opening (IVO)	-10° CA
Intake valve closing (IVC)	225° CA
Exhaust valve opening (EVO)	495° CA
Exhaust valve closing (EVC)	14° CA

SPARK DISCHARGE IN STEADY FLOW

The flow field around the spark gap has a profound effect on the spark discharge process as well as the flame kernel formation and flame propagation. In this chapter, the effect of steady flow velocity (henceforth called "mean flow" velocity) on the turbulence generated due to spark electrodes, and the spark discharge characteristics under flow conditions are investigated. All the empirical tests and the numerical simulations are performed at ambient pressure and temperature conditions. The flow field in the vicinity of the spark gap under steady cross-flow conditions is studied using a combination of PIV measurement and CFD simulation. The turbulence generated downstream of the spark plug is analyzed using two parameters, turbulent velocity and vorticity magnitude. The spark discharge characteristics under the effect of flow field are studied using discharge voltage and current profiles, and direct imaging of spark plasma channel. The discharge duration and frequency of restrikes are calculated and correlated with the flow velocity.

4.1 PIV Flow Field Measurement

The PIV image data processing method using PIVLab is discussed in Chapter 3. The ensemble averaged velocity vectors and flow streamlines for mean flow velocity of 2.5 m/s are presented in Figure 4.1. The presented velocity data is the average of 500 consecutive image frames, which corresponds to 50 ms of flow time interval. The large-scale flow structures generated in the wake of spark plug geometry can be observed clearly from the velocity vectors. The vortex formed as a result of the turbulence generated by the spark threads is marked as "1" in Figure 4-1. The effect of the gap between the ceramic insulation and the metal shell on flow field can be seen from the downward flow velocity immediately

downstream of the ceramic (indicated by “2” in Figure 4-1). This flow is of importance as it influences the heat transfer between the spark plug and the surrounding charge mixture.

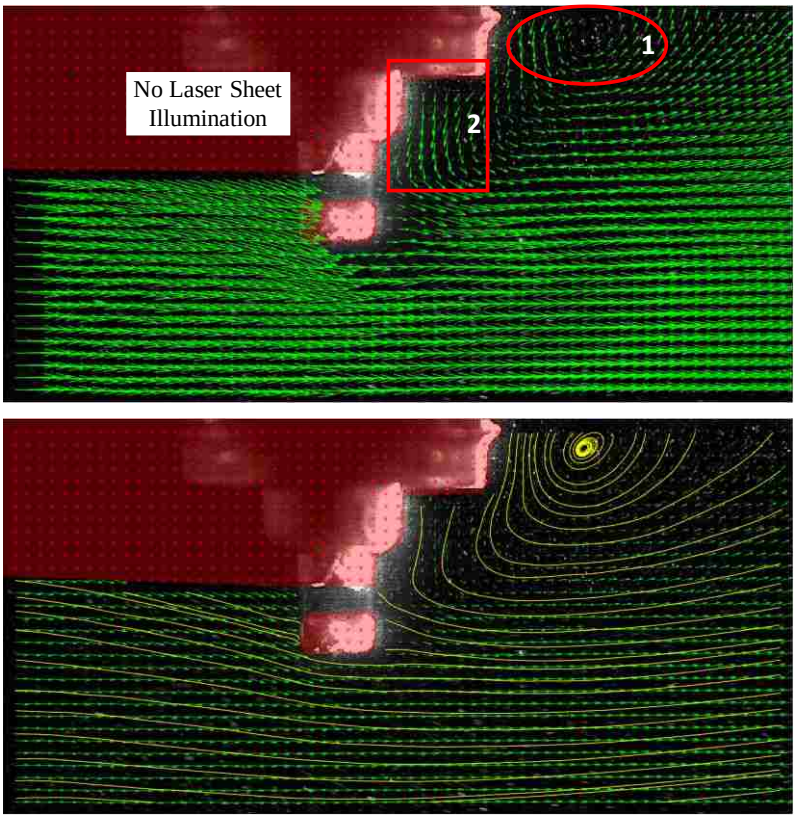

Figure 4-1. Ensemble averaged velocity vectors and streamlines for 2.5 m/s mean flow

Although, the majority of reflections can be removed by painting the spark plug black, the layer of paint itself can reflect a portion of light, which impacts the correlation calculation within the spark gap. As a consequence, the PIV correlation results in an erroneous velocity magnitude. While it is possible to manually calculate the overall flow speed and direction by tracking a particle across the image pairs, local flow field and small turbulent scales cannot be resolved. The mean of the manual velocity calculations across 10 image pairs results in a velocity of 3.07 m/s, which is slightly higher than the mean flow velocity. The slightly higher value is expected because of sudden contraction to the flow provided by the spark electrodes [63].

The velocity magnitude and small-scale vortex locations are shown in Figure 4-2. As expected, there is presence of velocity gradient downstream of the spark plug. Moving from point A to B (Figure 4-2) parallel to plug axis, velocity magnitude decreases progressively as the obstruction due to spark plug becomes larger. The spark gap offers minimum impediment to the flow whereas the spark thread, being the largest bluff body, provides maximum reduction in the velocity. Downstream of the spark plug, the velocity magnitude increases in the flow direction as the effect of bluff body (spark plug in this case) diminishes gradually. The flow downstream of the spark plug is highly distorted as a result of the presence of scattered turbulent structures, with most of the small-scale vortices being concentrated in the areas immediately before or after the presence of an obstacle.

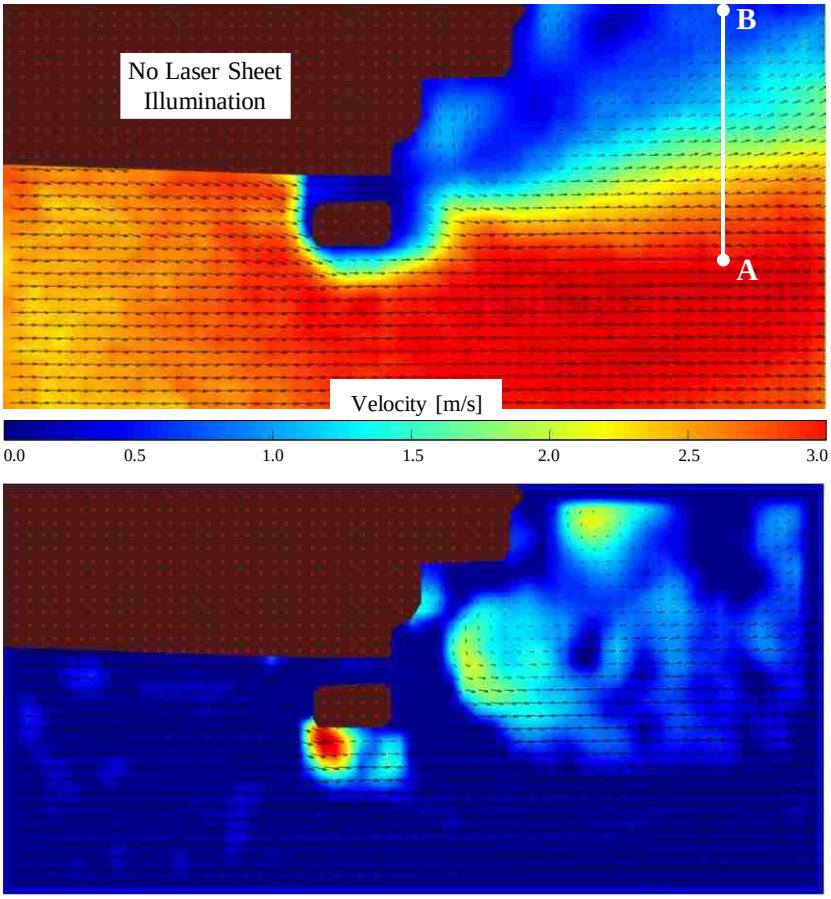

Figure 4-2. Velocity magnitude and small-scale vortex locations for 2.5 m/s mean flow

The instantaneous velocity vectors from three randomly chosen, consecutive image pairs are presented in Figure 4-3. While the ensemble averaged velocity can give an overall view of the vortex structures, instantaneous velocity shows the transient changes.

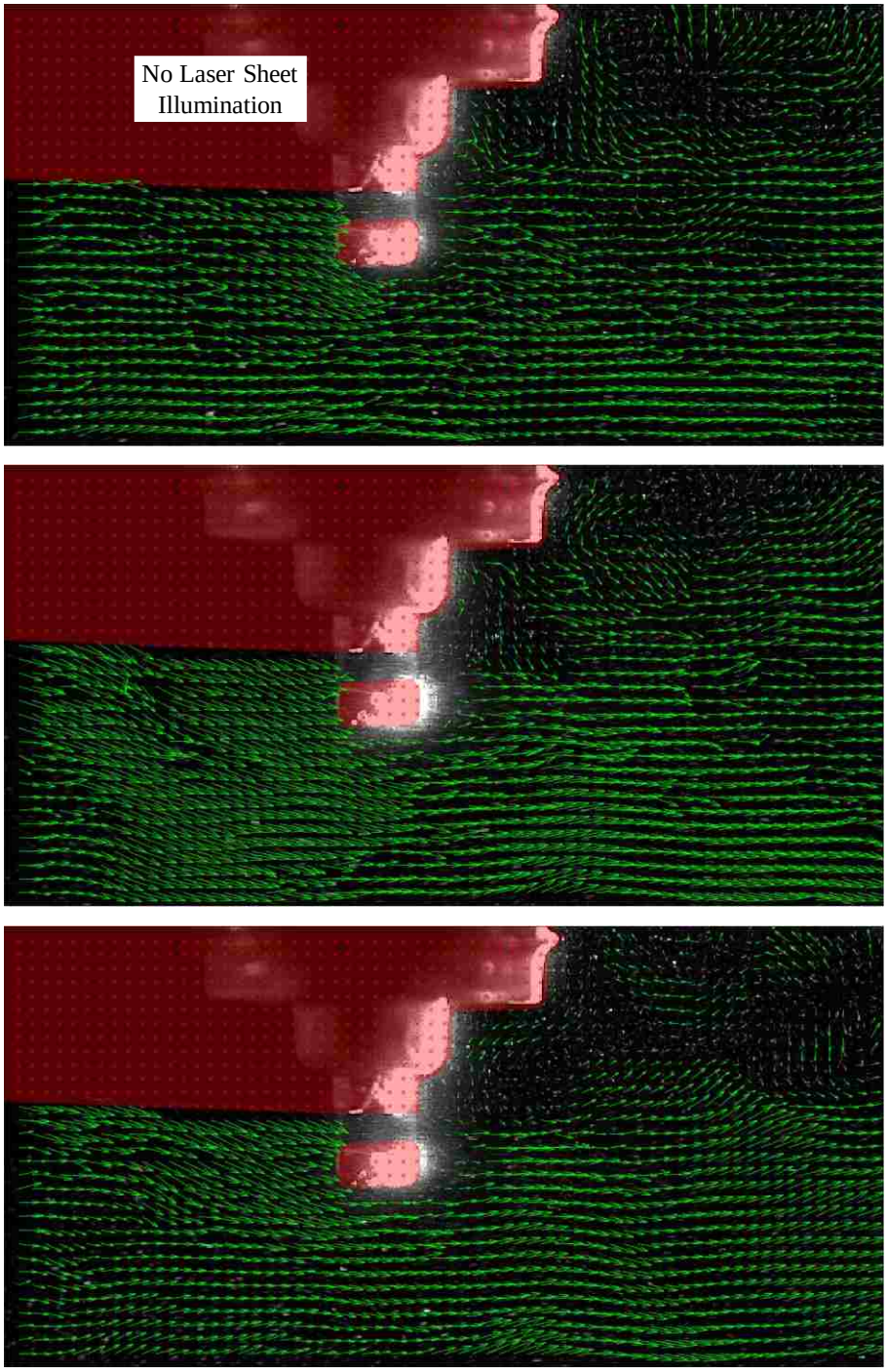

Figure 4-3. Instantaneous velocity vectors for 2.5 m/s mean flow

It is evident from the instantaneous vectors that although the overall flow field remains almost identical, with the presence of turbulent vortices and velocity gradient downstream of the spark plug, the vortex structures after the plug are subject to continuous formation and shedding.

A similar overall flow structure is observed at higher velocities, but the resolution of PIV measurement decreases because of the lower particle density at higher flow rates. Ensemble averaged velocity vectors, streamlines, velocity magnitude and small-scale vortex locations are shown in Figure 4-4 for a mean flow velocity of 5 m/s.

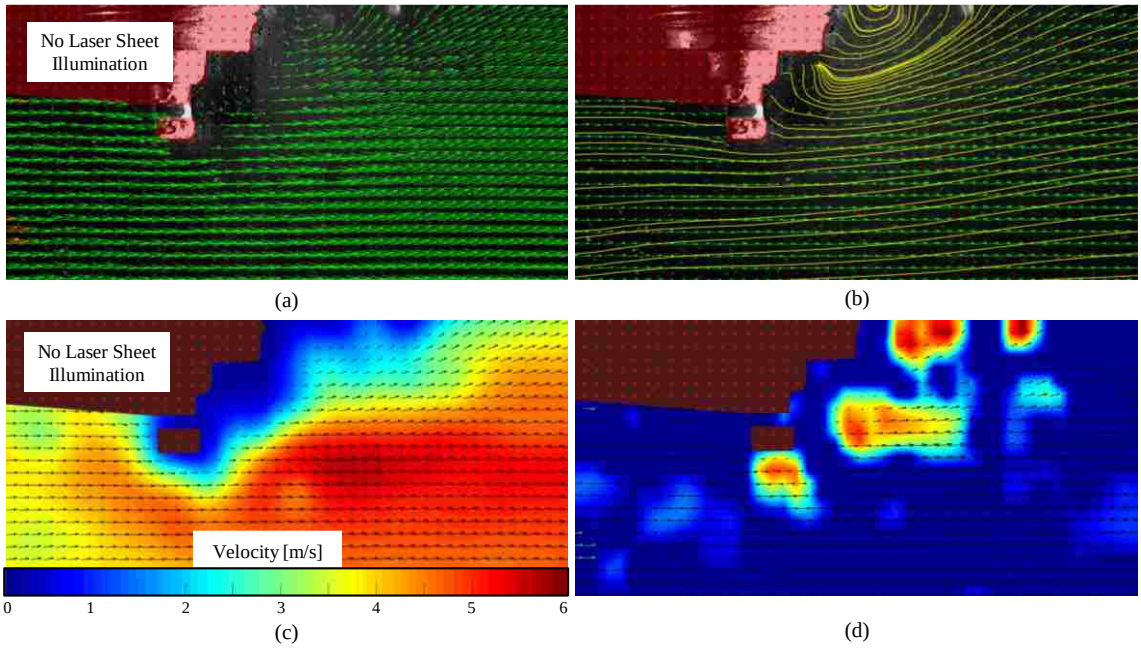

Figure 4-4. Ensemble averaged flow parameters for 5 m/s mean flow: (a) velocity vectors, (b) streamlines, (c) velocity magnitude, (d) small-scale vortex locations

The raw PIV images at a mean flow velocity of 6.8 m/s are presented in Figure 4-5. The spark channel ignites the olive oil particles in the flow. A “void” in the flow downstream of the spark channel can be observed because of the absence of the seeding particles. There seems to be a perceptible difference between the rate of spark stretch and the speed of the

"void" generated by the plasma channel. The separation between the spark and the void increases until it dissolves in the surrounding flow. The increasing separation between the spark channel and the void may suggest that the rate of the spark stretch is lower than the flow velocity across the spark gap.

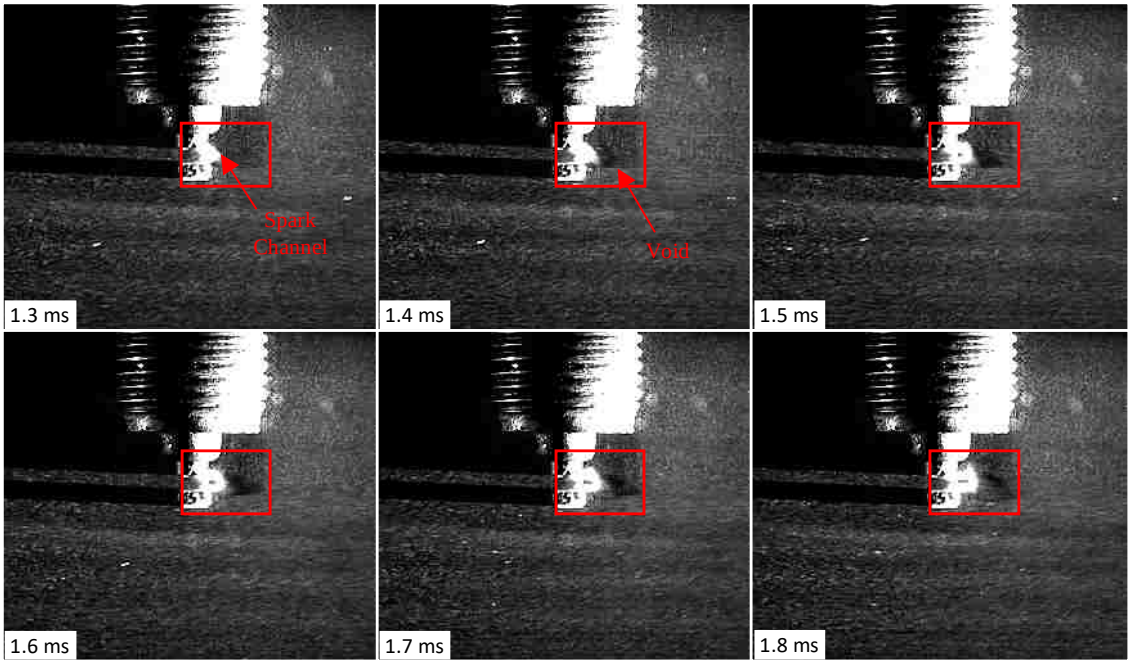

Figure 4-5. Raw PIV images with enhanced contrast under 6.5 m/s mean flow

4.2 Steady Flow Numerical Simulation

The data from the numerical simulations is post processed in ANSYS Ensight version 10.1. The mean flow velocity is varied from 2.5 m/s to 100 m/s. The lower flow velocity (2.5 m/s) case is used to validate the numerical model with PIV measurement data. The main flow parameters analyzed from the simulation data are the flow velocity, the turbulent velocity, and the vorticity near the spark gap. Average values of flow velocity and turbulent velocity are calculated in the spark gap over a cylindrical volume. The cylinder is 0.9 mm in diameter and 0.6 mm in height, with a volume of approximately 0.4 mm^3.

The turbulent velocity (u') is defined as the root mean square of the fluctuating velocity components. It is calculated from the turbulent kinetic energy (k) expression using equation 4.1 [62].

$$u' = \sqrt{\frac{2}{3}k} \tag{4.1}$$

The vorticity is mathematically defined as the curl of velocity vector. Physically, vorticity vector represents the number of rotations of an eddy per unit time. In the tensor form, vorticity is calculated using equation 4.2 [62].

$$\omega = \nabla \times \bar{u} = \left(\frac{\partial u_k}{\partial x_j} - \frac{\partial u_j}{\partial x_k}\right)\hat{\imath} - \left(\frac{\partial u_k}{\partial x_i} - \frac{\partial u_i}{\partial x_k}\right)\hat{\jmath} - \left(\frac{\partial u_j}{\partial x_i} - \frac{\partial u_i}{\partial x_j}\right)\hat{k} \tag{4.2}$$

Where, u_i, u_j and u_k are the x, y and z components of velocity respectively.

Since the spark gap experiences a highly turbulent flow inside the engine, Reynolds number (Re) is calculated for the chosen velocity values to ensure that the flow in the rectangular channel, upstream of the spark plug, remains in the turbulent regime during the steady cross-flow tests or the simulation. The Reynolds number is a non-dimensional parameter, defined as the ratio of the inertial forces to the viscous forces. It is used as a measure to predict if the flow is laminar or turbulent and is calculated from the fluid density (ρ) and dynamic viscosity (μ), mean flow velocity ($\bar{U}$) and characteristic hydraulic diameter (d) using equation 4.3 [64].

$$Re = \frac{\rho . \bar{U} . d}{\mu} \tag{4.3}$$

As illustrated in Figure 4-6, the Reynolds number for all the chosen flow velocities is higher than 4000, which indicates that a fully developed turbulent flow exists upstream of the

spark plug. A comparison between the velocity distribution from the numerical simulation and the PIV measurement for a mean flow velocity of 2.5 m/s is presented in Figure 4-7.

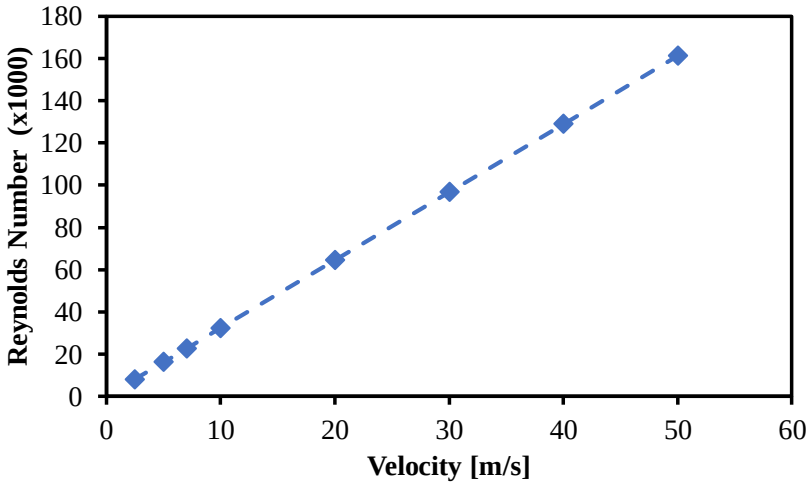

Figure 4-6. Reynolds number of the flow upstream of spark plug

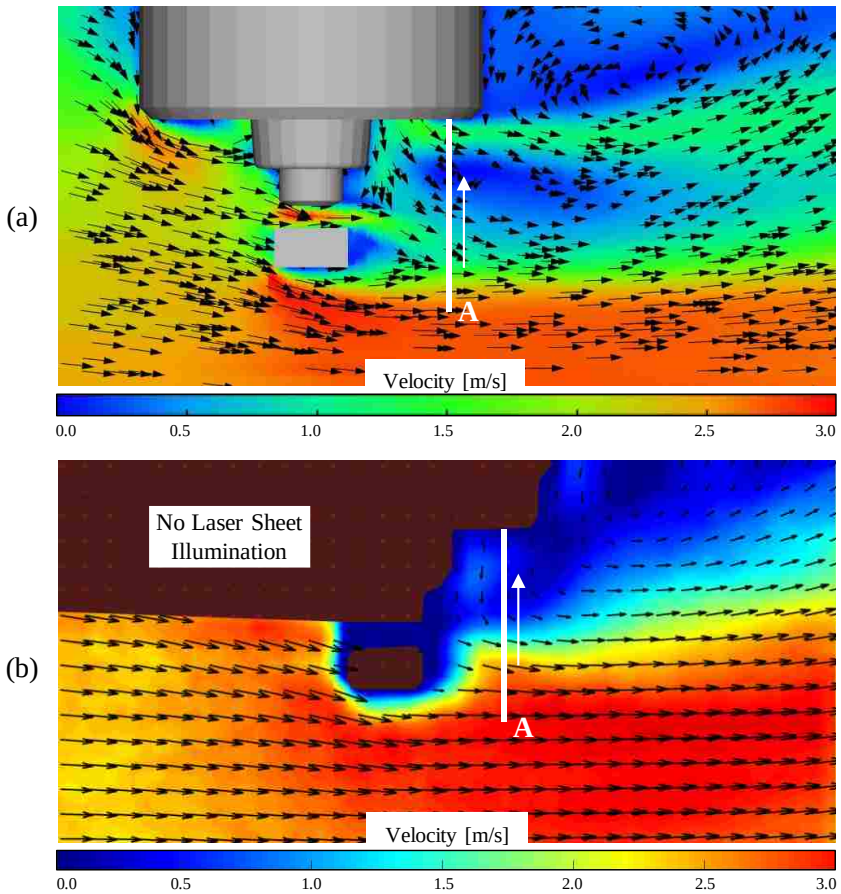

Figure 4-7. (a) Numerical and (b) empirical velocity contours for 2.5 m/s mean flow

The velocity profiles from the numerical simulation and the PIV measurements show a good agreement. The comparison of the simulated and empirical flow velocity on a 10 mm linear section, taken 5 mm downstream of the spark gap (indicated by the white line in Figure 4-7) is presented in Figure 4-8. The maximum difference between the empirical and simulated velocity magnitude is 12% (0.38 m/s), with numerical simulation underpredicting the velocity magnitude. However, the overall trend in both cases is similar. Major difference can be observed within and near the spark gap. As discussed earlier, the reflections during the PIV measurements impedes a reliable measurement of velocity in the gap. Therefore, the velocity distribution (Figure 4-7(b)) shows a very low velocity across the spark gap. However, the manually calculated velocity magnitude of 3.07 m/s in the gap (for 2.5 m/s mean flow velocity) is similar to the simulated value. Therefore, the model is considered acceptable for the study of flow field at higher cross-flow velocities.

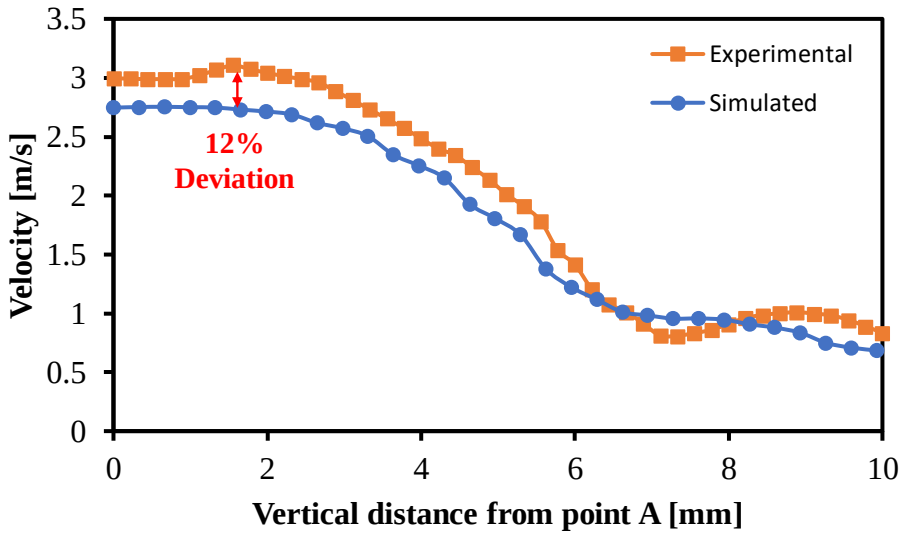

Figure 4-8. Simulated and empirical velocity at 5 mm downstream of spark gap

The mean flow velocities of 10 to 100 m/s at ambient conditions are studied using the numerical simulations. The velocity distribution for the flow fields corresponding to the

inlet velocities of 10, 20, 50 and 100 m/s are shown in Figure 4-9. The flow field in between the ceramic insulator and the outer metal shell is also simulated. This flow influences the heat exchange between the spark plug and the in-cylinder charge. The velocity distribution downstream of the spark plug shows a similar trend for all the simulated flow fields. The overall flow velocity throughout the domain increases with the increase in the inlet flow speed. Within the spark gap, the flow velocity is higher than the mean streamwise velocity for all cases. This can potentially be attributed to the flow acceleration because of the contraction provided by the spark electrodes. A comparison between the gap velocity and the mean flow velocity is presented in Figure 4-10. The difference between the two velocities increase as the mean flow velocity increases. The difference is 0.64 m/s at the mean flow velocity of 2.5 m/s, which increases to 27.72 m/s at the 50 m/s mean flow velocity. This difference further supports the influence of the contraction, as according to flow continuity and Bernoulli's principles, the difference in velocity due to sudden contraction is proportional to the incoming flow velocity [64]. These results agree with the previous investigation of the flow velocity across the spark gap performed by Halldin using laser doppler velocimetry (LDV) [26].

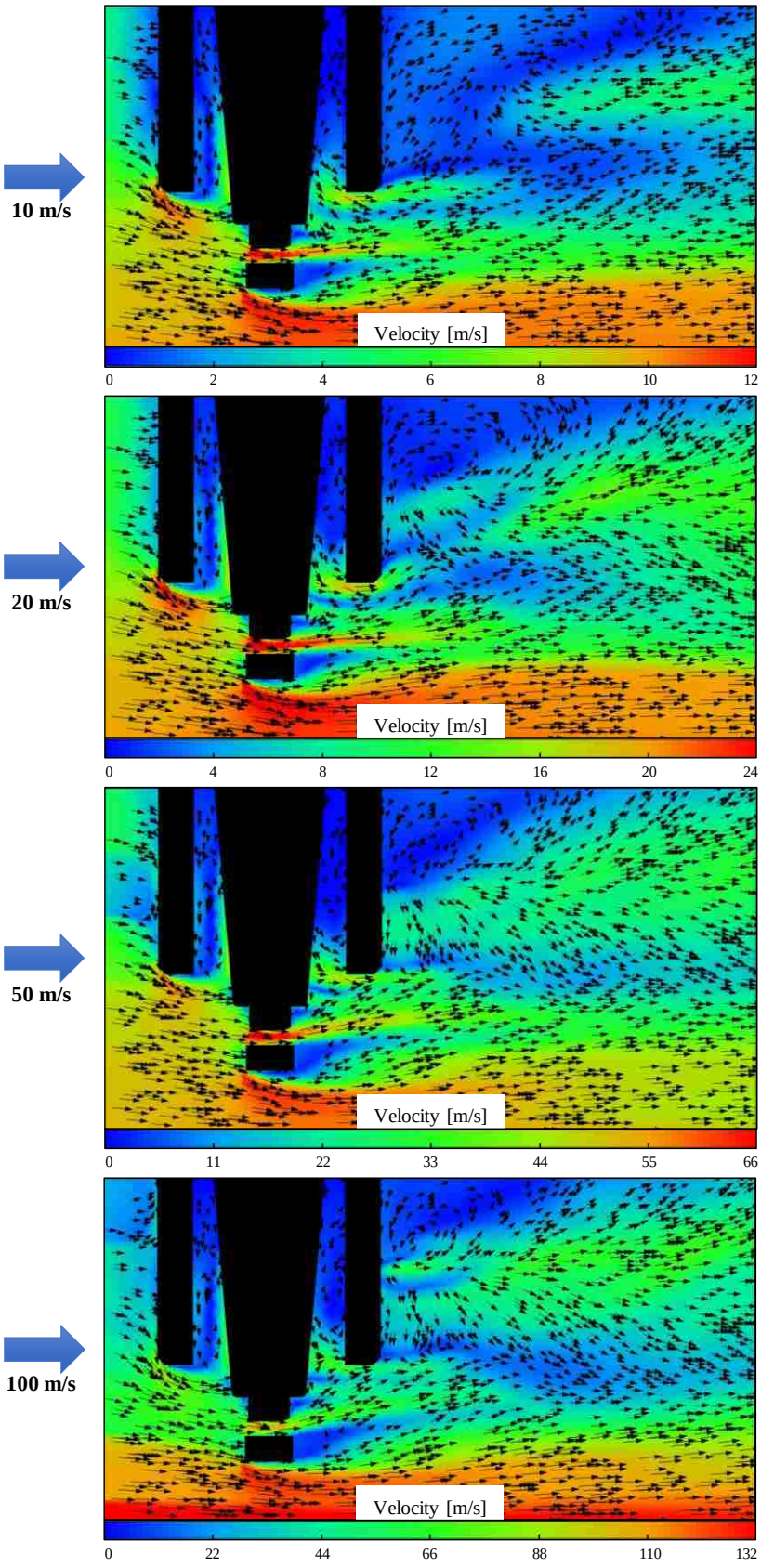

Figure 4-9. Velocity distribution at 10, 20, 50 and 100 m/s mean flow velocities

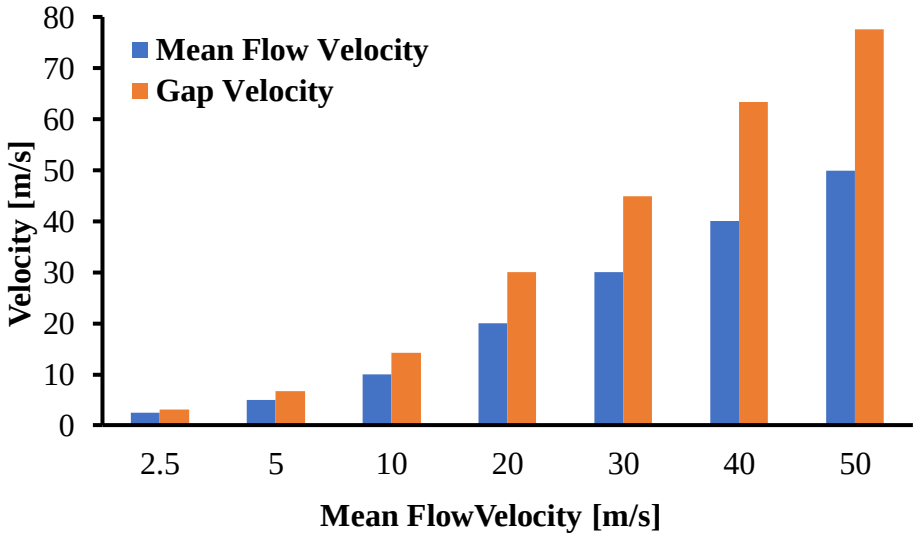

Figure 4-10. Mean flow velocity and gap velocity comparison

While the flow velocity across the spark gap has significant effect on the spark event, turbulence influences the initial flame kernel formation and flame propagation. The turbulent velocity and vorticity magnitude are the two parameters used to study the flow turbulence. Downstream of the spark gap, the flow is highly turbulent, and the turbulence increases with the mean flow velocity. The turbulence dissipates progressively as the flow moves away from the plug. This is evident from the turbulent velocity and vorticity contours illustrated in Figure 4-11. The turbulent velocity and the vorticity magnitude increases with the mean flow velocity.

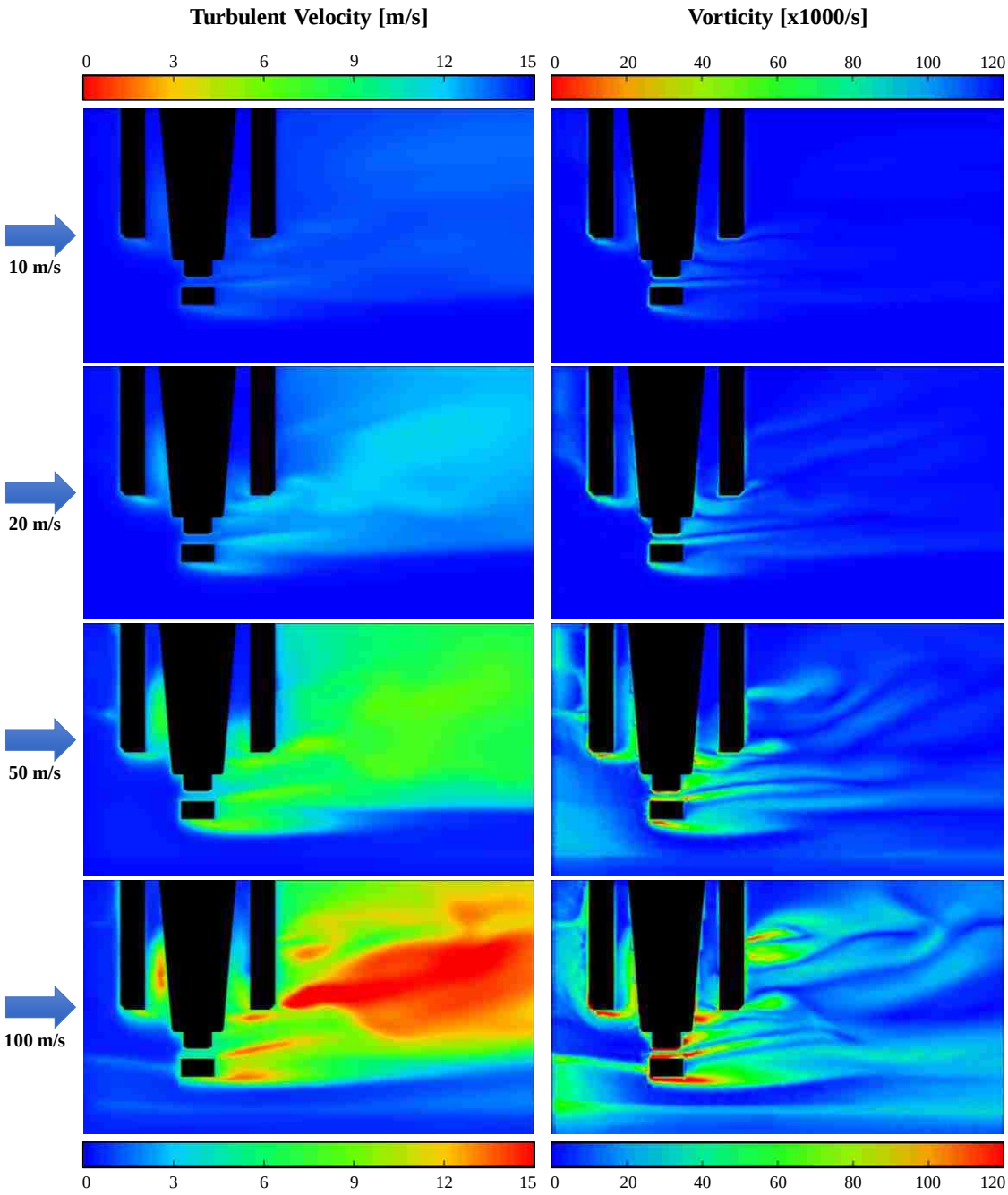

Figure 4-11. Turbulent velocity and vorticity contours for 10, 20, 50 and 100 m/s mean flow velocities

The turbulent velocity and vorticity magnitude, within and downstream of the spark gap, at different inlet flow speeds is illustrated in Figure 4-12 and Figure 4-13 respectively.

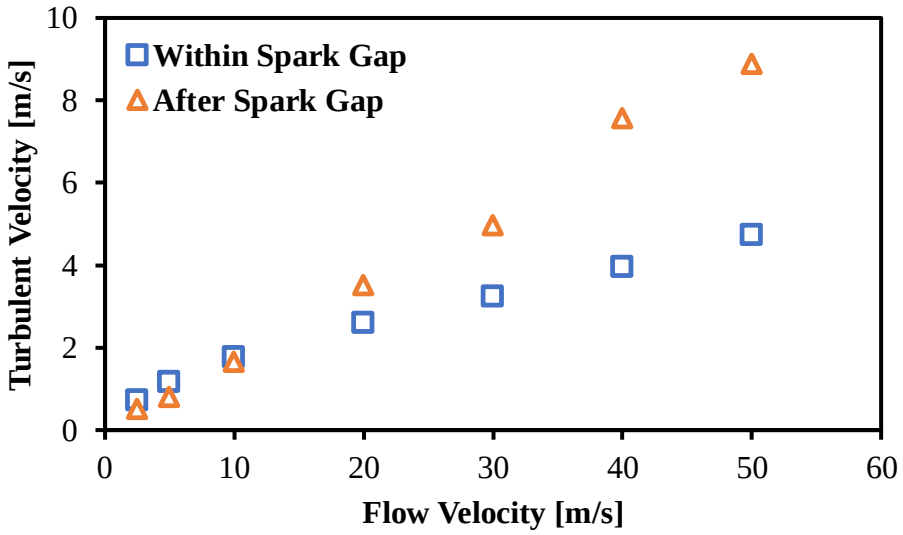

Figure 4-12. Average and maximum turbulent velocity within and after the spark gap

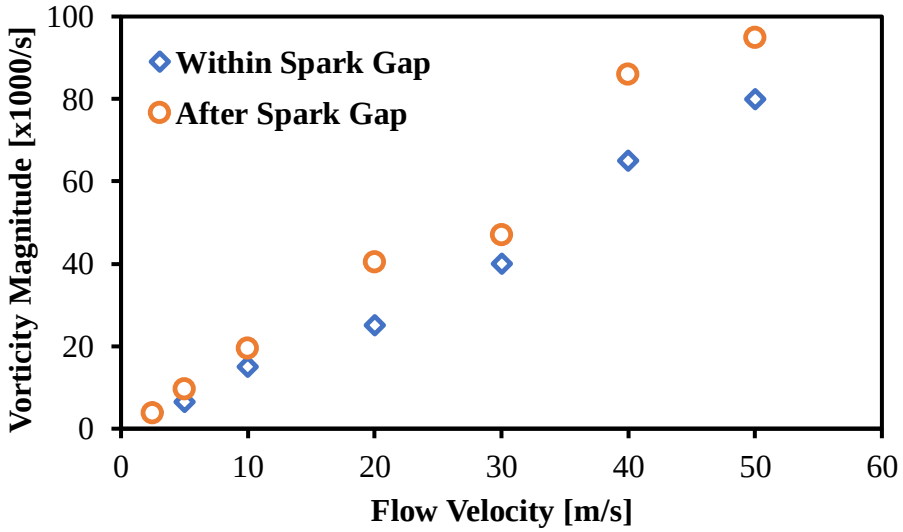

Figure 4-13. Vorticity magnitude within and after the spark gap

As demonstrated in the contour plots (Figure 4-11), the turbulent velocity (Figure 4-12) and the vorticity magnitude (Figure 4-13), within the spark gap, the flow has high velocity and a relatively low turbulence. Whereas, immediately downstream of the spark gap, the

flow velocity is lower, and the turbulence is relatively higher. Similar results have been obtained by Kim et al. in their investigations of the flow velocity and turbulence near the spark gap under a steady cross-flow using the hot wire anemometry technique [41].

It has been reported by the researchers that the combustion initiation and the initial flame propagation can be enhanced by a relatively low velocity and high turbulence conditions [26,42-44]. Hence, the charge mixture conditions immediately downstream of the spark plug can potentially offer a better background for the combustion initiation and flame propagation as compared to the conditions within the spark gap.

4.3 Spark Discharge under Steady Cross-Flow

As discussed earlier in the literature review, in addition to enhancing the flame propagation, the in-cylinder flow has a significant effect on the spark discharge process. To decouple the flow effect from other influencing parameters, the spark discharge under cross-flow is studied outside the engine, in the ambient conditions. The electrical circuit and the direct imaging system are discussed in Chapter 3. The spark area is calculated by converting the raw greyscale images of the spark channel into binary images using a MATLAB code. In the binary images, the spark area is represented as the white pixels (1) and background is converted into black pixels (0). The threshold for the binary conversion is carefully determined by comparing the processed binary and raw images to ensure that the spark channel is completely included in the white section. The area of each pixel is determined through calibration. The spark area is finally calculated by multiplying the total number of white pixels to the area of a single pixel.

Under quiescent (no flow) conditions, a steady arc between the spark electrodes is maintained after the breakdown phase. The discharge characteristics under quiescent

conditions, along with the plasma channel images are illustrated in Figure 4-14. The voltage remains almost constant at approximately 470V during the glow phase. The discharge current gradually decays, and the total discharge duration is 2.4 ms. The spark plasma is confined within the spark electrodes throughout the duration of discharge and its intensity diminishes as the current level decreases.

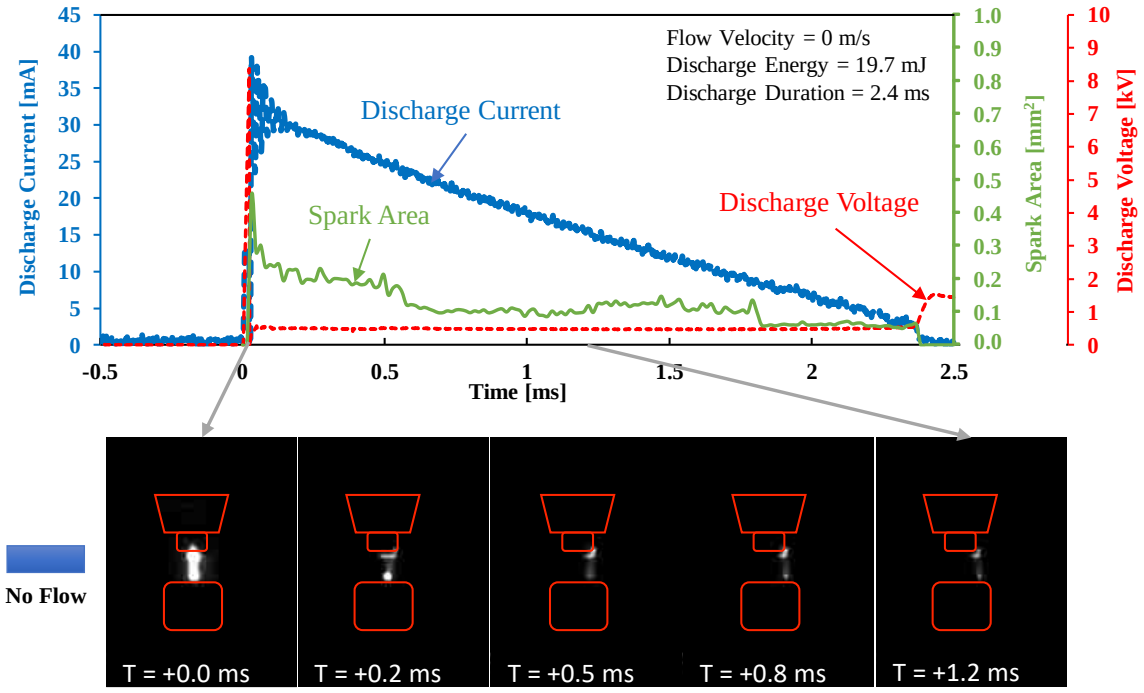

Figure 4-14. Spark Plasma under quiescent conditions

Under the effect of flow, the spark plasma is stretched in the flow direction. Eventually, the stretched plasma breaks and spark restrikes are. As opposed to the quiescent conditions, the discharge voltage is no longer constant, but increases gradually and then suddenly drops in response to the spark restrike. This behavior becomes increasingly frequent as the discharge current diminishes near the end of the spark discharge. The discharge characteristics under low mean flow velocities of 5 and 10 m/s are presented in Figure 4-15 and the effect of higher flow velocities (20 and 40 m/s) is demonstrated in Figure 4-16.

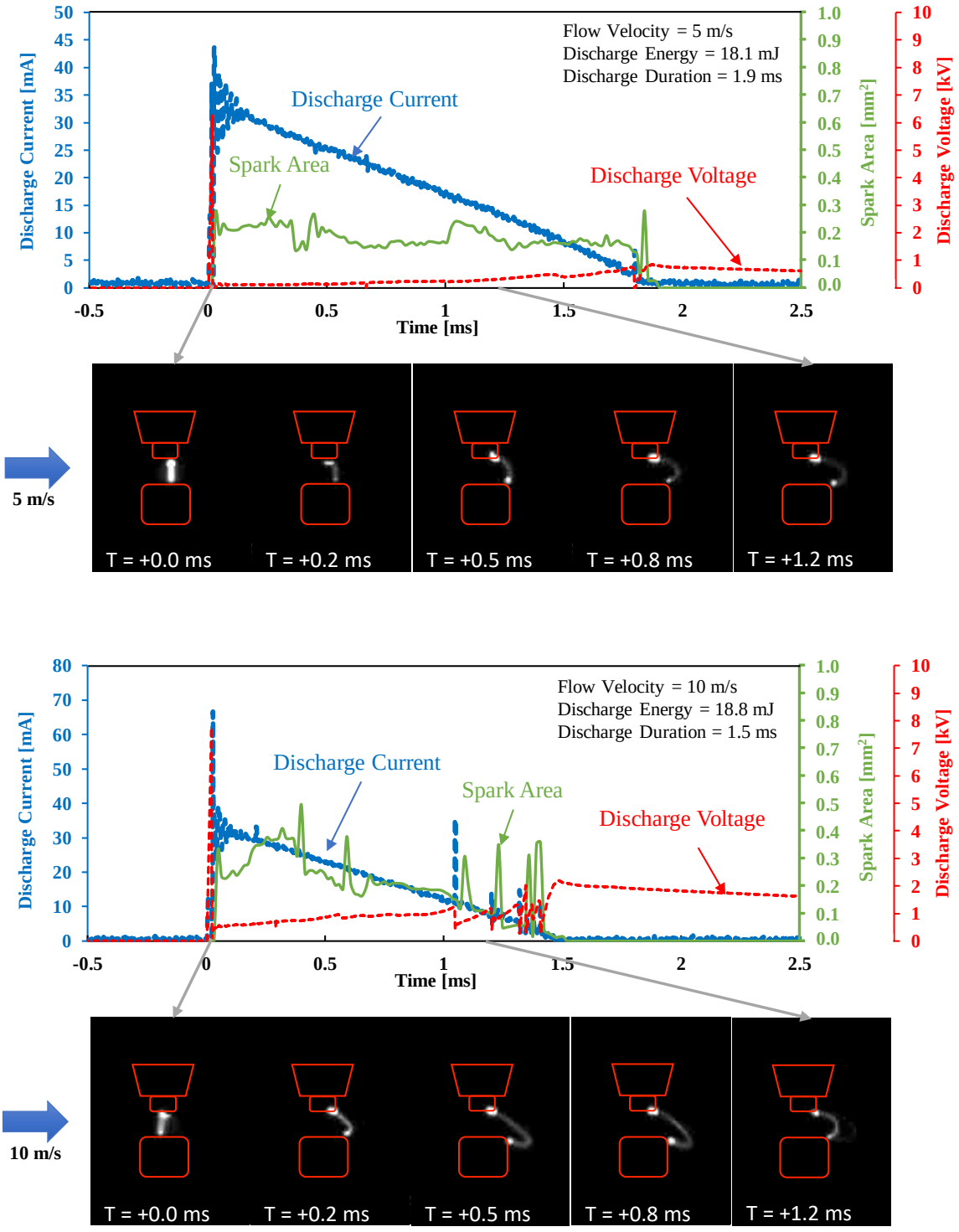

Figure 4-15. Spark plasma under 5 m/s and 10 m/s mean flow velocities

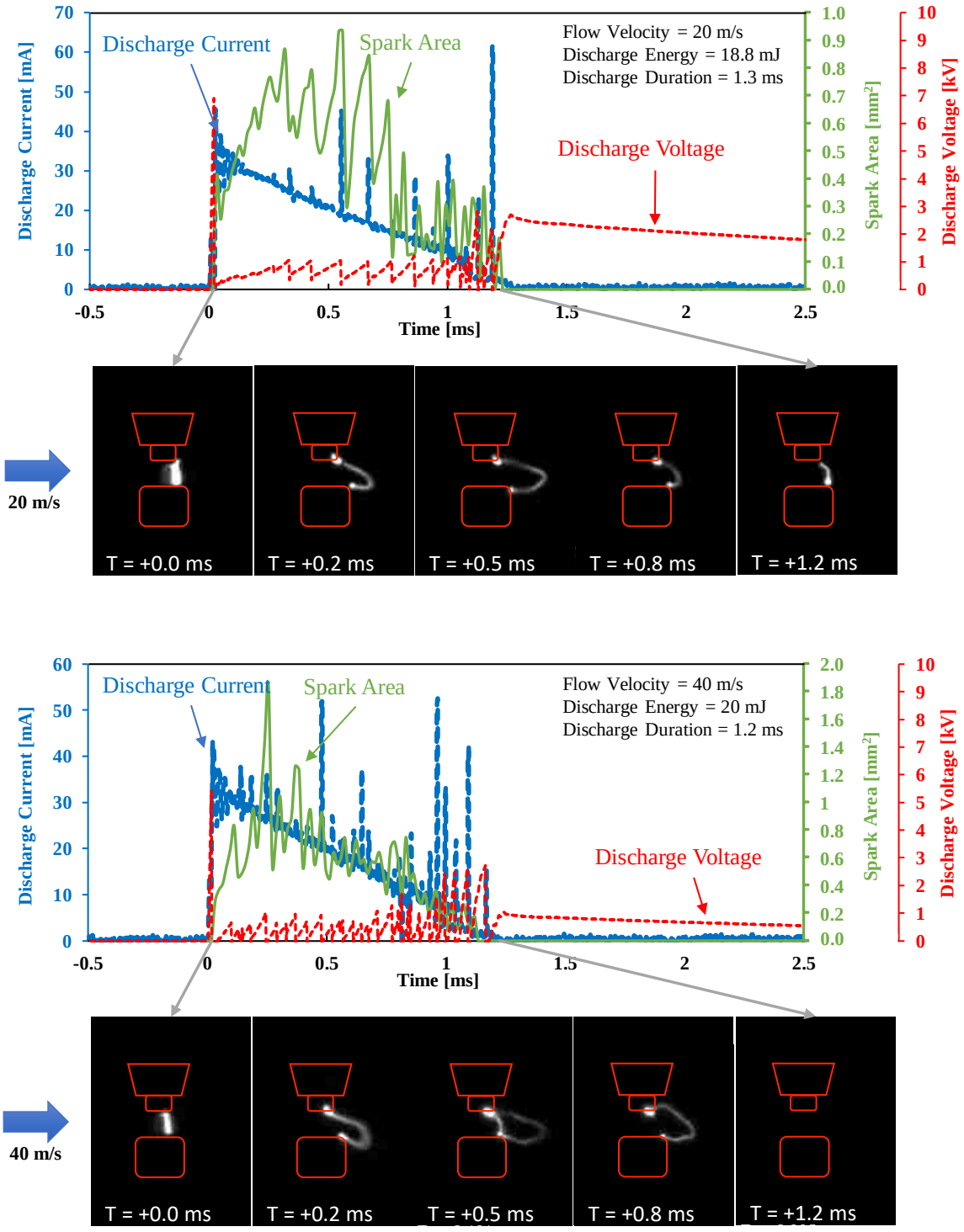

Figure 4-16. Spark plasma under 20 m/s and 40 m/s mean flow velocities

The flow across the spark gap has a negligible effect on the breakdown phase, owing to the very small duration (in the order of hundreds of nanoseconds) of the breakdown phase. Hence, as illustrated in Figure 4-17, the breakdown voltage and the peak current stays the same across the whole flow velocity range tested. The peak current in the figure refers to the maximum current at the start of the glow phase. The presented data is an average of 30 test points at each velocity and the error bars represent the standard deviation in the results.

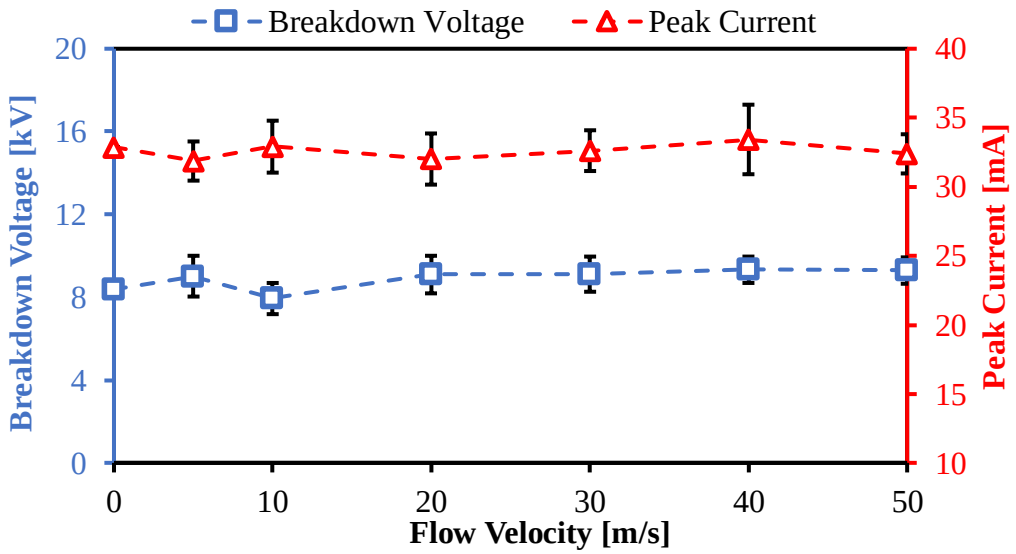

Figure 4-17. Breakdown voltage and glow phase peak current at different mean flow velocities

For all the tested conditions, the breakdown voltage remains around 8 kV and the glow phase peak current is approximately 30 mA immediately after the breakdown. The spark lengths at flow velocities of 5, 10, 20 and 40 m/s are shown in Figure 4-18. With an increase in the mean flow velocity, spark stretch as well as the rate of spark stretch increases. This behavior can additionally be observed from the spark channel images as well as the spark area traces presented in Figure 4-15 and Figure 4-16. The rate of spark stretch is represented by the slope of the spark length vs time plot. A sudden drop in spark length is an indicator of the spark plasma restrike. As observed from the raw PIV images in Figure 4-5, even

though the rate of spark stretch increase with the increase in flow velocity, it still remains lower than the flow velocity. The spark stretch rate calculated from the plasma length before the first restrike agrees with the observation from the PIV images. At the mean flow velocity of 5 m/s, initial spark stretch rate is calculated to be 1.2 m/s, which increases to 2.4 m/s at 10 m/s, 9.4 m/s at 20 m/s and further 33.8 m/s at 40 m/s flow velocity.

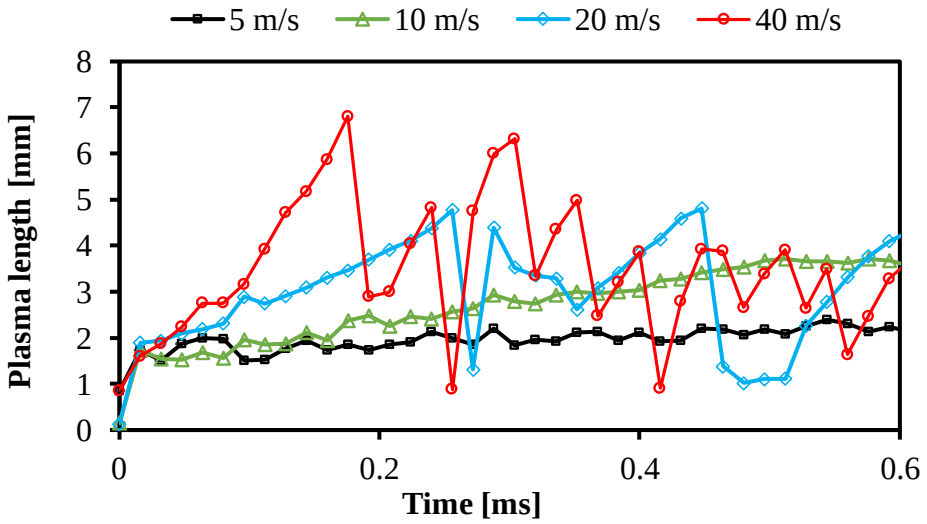

Figure 4-18. Spark length at 5, 10, 20 and 40 m/s mean flow velocities

The discharge duration reduces with the increase in the flow velocity. At quiescent conditions, the total discharge duration is 2.4 ms, which is reduced to 1.5ms at 10 m/s flow velocity. A further reduction to 1.2 ms is seen at 40 m/s flow velocity. This reduction can be attributed to a higher energy dissipation because of the restrike events. As the restrike frequency increases, the energy dissipation also increases. Consequently, the discharge duration decreases as the flow velocity increases. However, the reduction is not linear. The duration decreases sharply at lower flow velocities and at higher flow velocities, the reduction is minimal. The discharge duration at different flow velocities is presented in Figure 4-19.

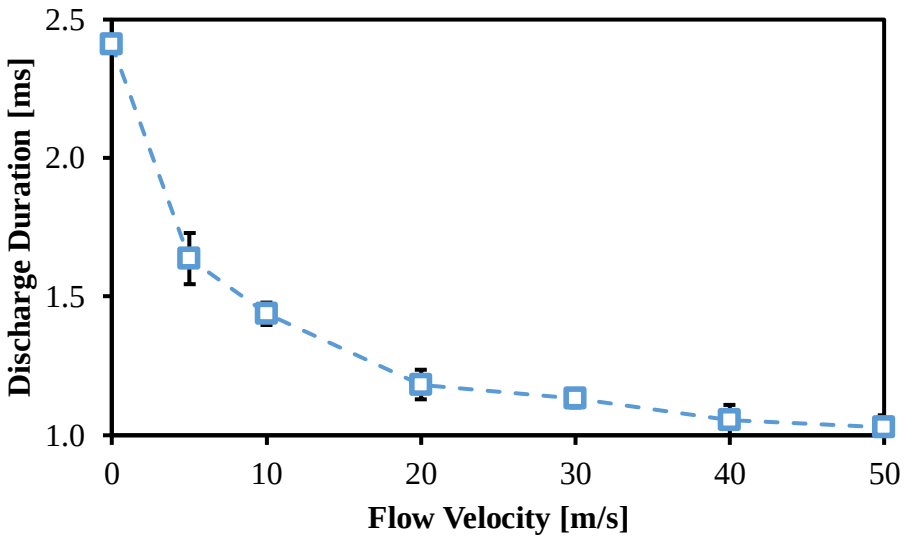

Figure 4-19. Discharge duration at different flow velocities

At the lowest tested velocity of 5 m/s, the spark stretch length increases gradually and eventually a restrike is evident 1.8 ms after the spark breakdown when the voltage across the electrodes cannot sustain the increased channel resistance. Only one restrike is seen at 5 m/s. The number of restrikes increases to 6 for 10 m/s, 12 at 20 m/s and further to 25 at 40 m/s flow velocity. Hence, the restrike frequency increases with an increase in flow velocity. The number of restrikes during a single spark event as well as the restrike frequency is illustrated in Figure 4-20. Moreover, with an increase in flow velocity, the first restrike happens closer to the spark breakdown and at a higher discharge current level. A higher discharge current level is required to sustain the spark channel longer at higher flow velocities. This behavior is evident from the time and the discharge current level at first restrike event for different flow velocities shown in Figure 4-21.

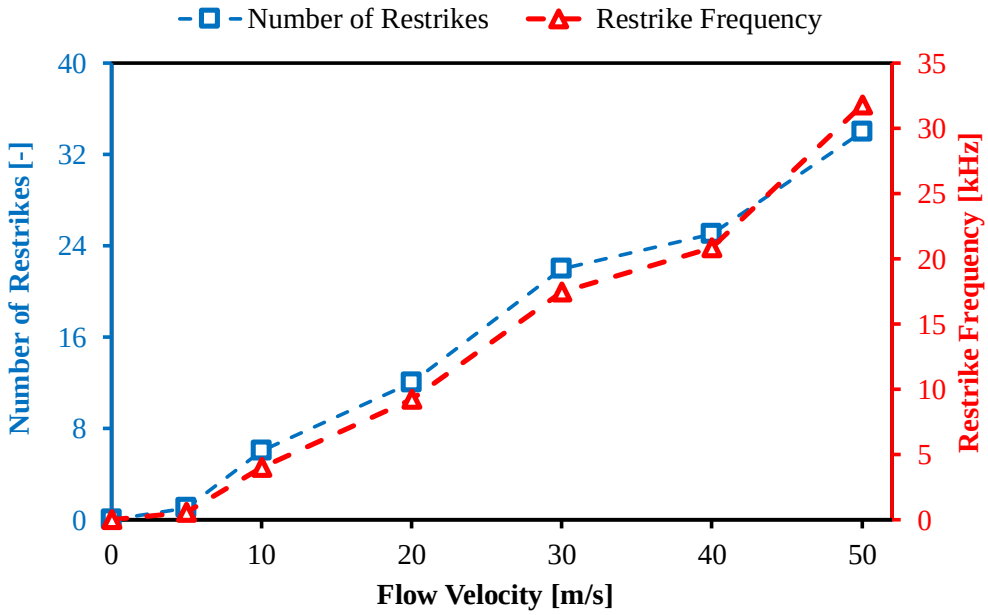

Figure 4-20. Number of restrikes and restrike frequency at different flow velocities

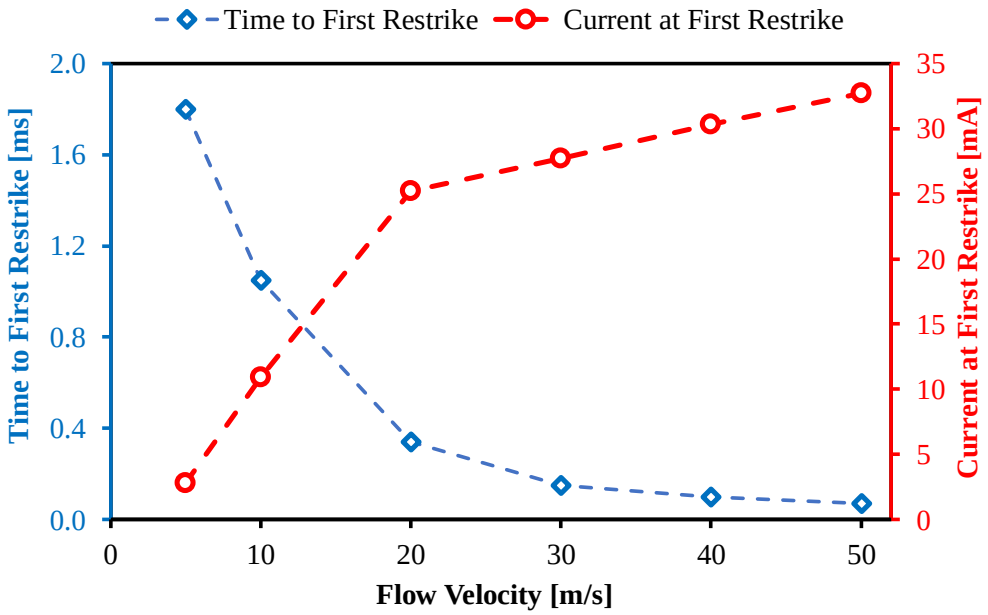

Figure 4-21. Time and current at first restrike for different flow velocities

It has been reported that boosting the discharge current levels, either an overall higher discharge current or a “constant” current profile, can help in reducing the frequency of restrike events [28,32]. The overall higher discharge current profile can sustain the initial stretch for a longer duration whereas the constant current profile improves the discharge characteristics in flow field throughout the spark event, especially near the end of the spark discharge.

From the flow field and the spark response results in steady cross flow, it is clear that flow velocity influences both turbulence in the wake of the spark gap and the spark plasma channel. While the flow across the spark gap helps in stretching the spark channel into the potentially favorable high turbulence and low velocity zone, this stretch may not be maintained long enough for a self-sustaining flame kernel to develop, especially at higher flow velocities or low discharge current levels. Once a flame kernel is successfully developed, a higher turbulence can enhance the further flame propagation. Therefore, there may exist an optimal flow velocity for a given discharge current level, where both the effects are balanced, and a better ignition behavior may be observed.

The spark channel response to the flow field remains very consistent for similar flow velocity conditions. The researchers have investigated the use of this response to estimate the velocity changes during the engine conditions [41,51-55]. Next chapter discusses the use of the spark anemometry as a diagnostic technique for the velocity estimation during the engine operation.

SPARK ANEMOMETRY

Based on the spark plasma behavior under a steady cross-flow, it can be observed that a correlation exists between the spark discharge characteristics and the flow velocity. It is possible to estimate the changes to the flow velocity across the spark gap during the engine operation from certain discharge parameters, namely the discharge duration and the restrike frequency. In this chapter, the use of spark anemometry as a diagnostic tool to study the variations in the flow velocity within the spark gap during engine operation is investigated. Due to the lack of an optical access into the engine cylinder, the flow velocity near the spark plug is estimated using the CFD simulations. The numerical simulation and the spark discharge characteristics measurements are performed at the engine motoring (i.e. no combustion) conditions to decouple the effects of fuel, residual gas fraction, and the thermal background because of combustion. The discharge current and voltage profiles are recorded during the ignition timing window (305° to 355° CA) at different air mass flow rates. Thereafter, the discharge duration and restrike frequency are used to estimate the gap velocity changes. The results are compared to the simulated velocity magnitude.

5.1 Flow Velocity in the Spark Gap

The parameters and the engine geometry used for the numerical simulation setup are discussed in Chapter 3. The simulation data is post-processed in ANSYS Ensight 10.1. Owing to the lack of an optical access into the engine, or a stable probe-based measurement system, direct velocity measurement during the engine operation is not possible. The CFD simulations of engine motoring at different mass flow rates is used to calculate the flow velocity in the spark gap during the ignition timing window. The gas exchange process for

the CFD simulation is validated using the empirical and simulated in-cylinder pressure traces. The comparisons of the simulated and measured pressure traces at intake mass air flow (MAF) rates of 3.53, 4.85 and 5.56 g/s are shown in Figure 5-1.

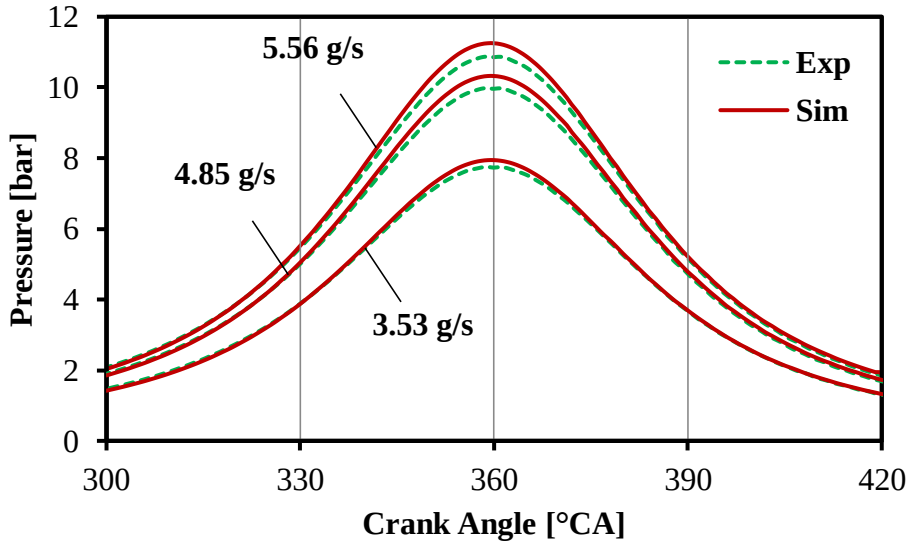

Figure 5-1. Comparison of empirical and simulated in-cylinder pressure traces

A maximum deviation of 0.5 bar is observed in the maximum in-cylinder pressure values near the top dead center (TDC). The compression and expansion stroke pressures show a good agreement. The deviation near the TDC can potentially be attributed to a combination of the crevice volume and the blow-by effects. During the engine simulation, the effects of the crevice volume (i.e. the volume between the cylinder wall and the piston, above the piston rings and below the piston crown) and blow by (i.e. the escaping of expanding gas mixture past the piston into the crankcase) are neglected, whereas during the empirical tests, they may influence the in-cylinder pressure.

The flow velocity in the spark gap is calculated as the average of velocity magnitude values over a cylindrical volume with same diameter as the spark electrode within the spark gap. Flow velocity is calculated in 10° CA increments during the ignition timing window of

305° to 355° CA. These crank angles correspond to the spark breakdown timings for the empirical measurements of the discharge characteristics during the engine operation. The in-cylinder flow field is analyzed in two viewing planes. The overall in-cylinder flow field is presented in the “center plane”, which passes through the center of engine cylinder along the cylinder axis. The flow in the spark vicinity is discussed in the “gap plane”, which passes through the spark gap, parallel to the spark plug axis. Both the viewing planes are shown in Figure 5-2.

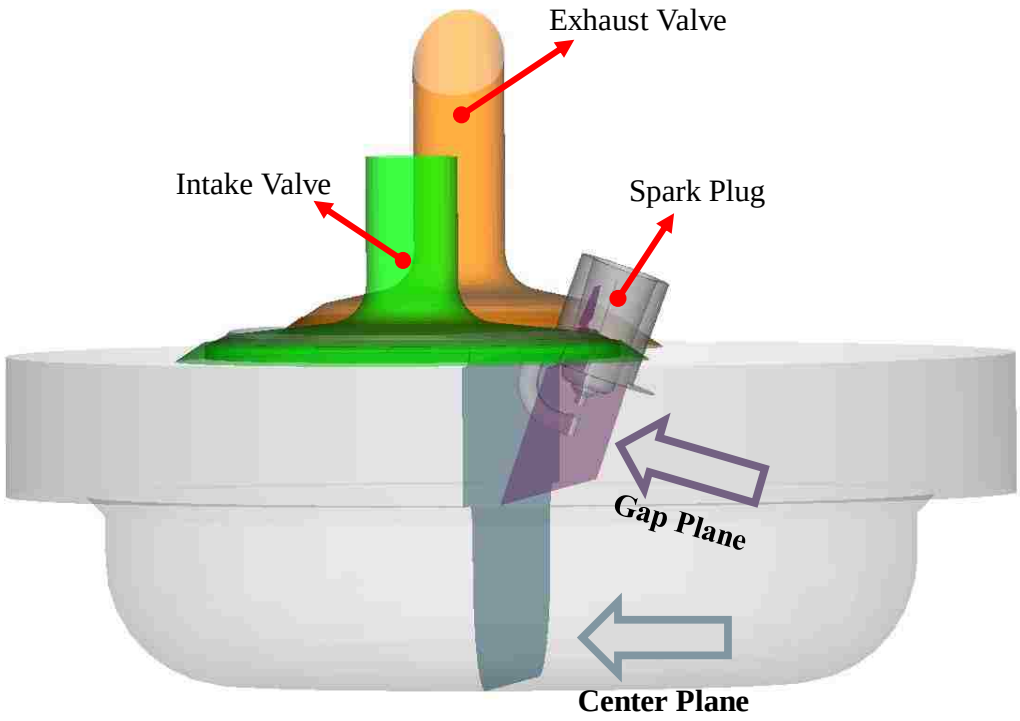

Figure 5-2. Viewing planes for in-cylinder flow field

The velocity magnitude in the spark gap at different mass flow rates is presented in Figure 5-3. The overall trend of the velocity magnitude within the spark gap remains similar for

all the simulated air mass flow rates. Increasing the mass flow rate results in a marginal increase in the flow velocity across the spark gap.

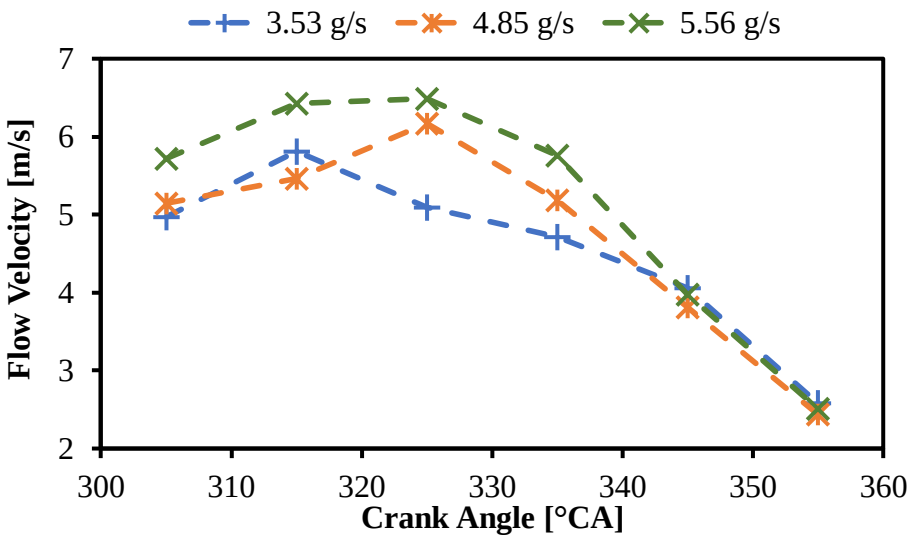

Figure 5-3. Simulated flow velocity in the spark gap during engine motoring

The velocity magnitude initially increases slightly and then gradually decreases as the compression stroke progresses. This behavior can be explained by the overall in-cylinder and spark vicinity flow field for 5.56 g/s intake MAF, illustrated in Figure 5-4 and Figure 5-5. At 315° CA, a low velocity vortical region, marked by red circle in the velocity contours, is developed near the center of cylinder as a result of the global swirl and tumble motion. This vortex moves towards the cylinder head as the compression stroke progresses. The effect of this low velocity vortex on the flow within the spark gap becomes more pronounced as the piston approaches TDC and the available volume for the air motion is reduced (Figure 5-5). The in-cylinder flow profile remains similar for other simulated MAF conditions as well.

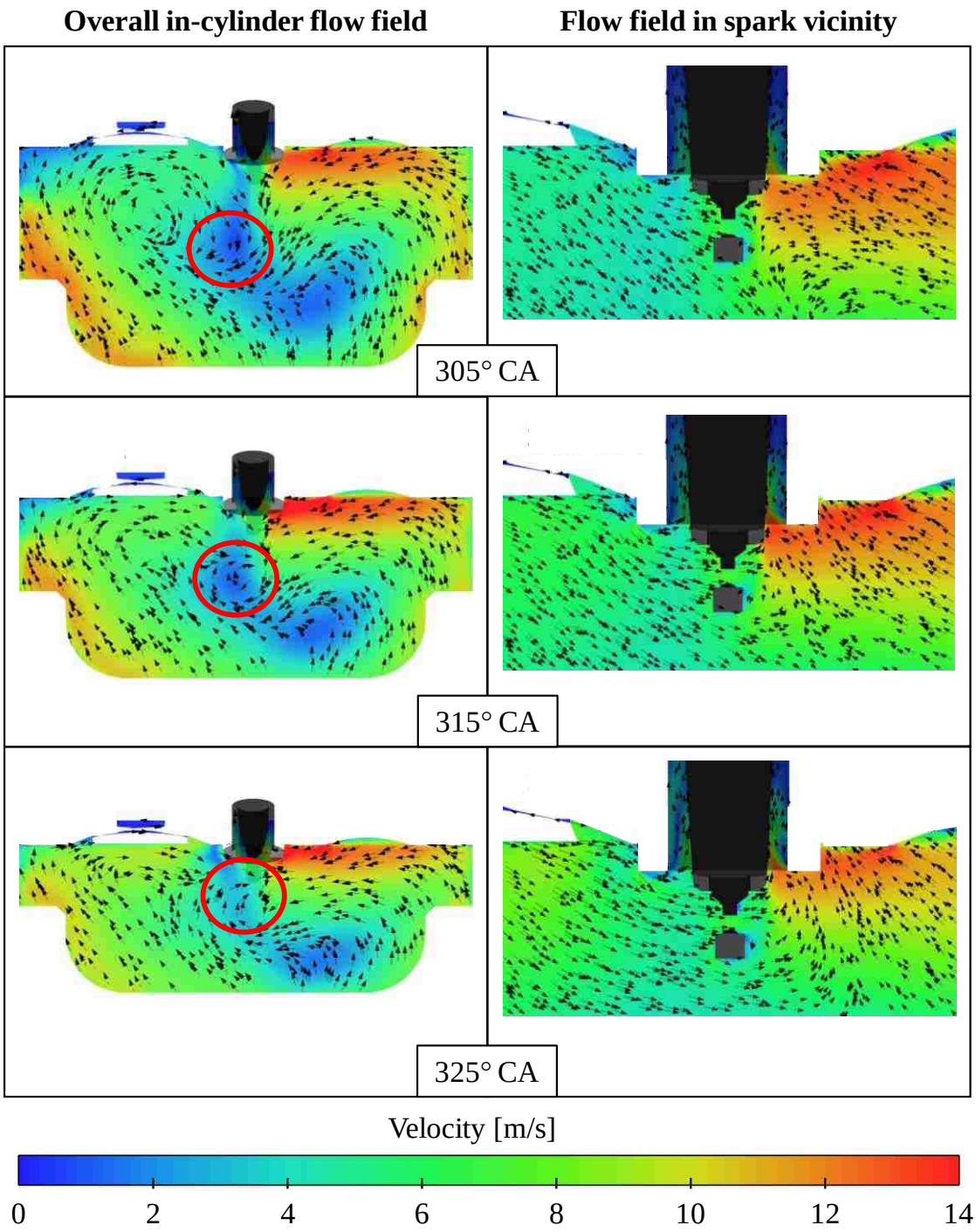

Figure 5-4. Overall in-cylinder and spark vicinity flow field at 5.56 g/s intake MAF

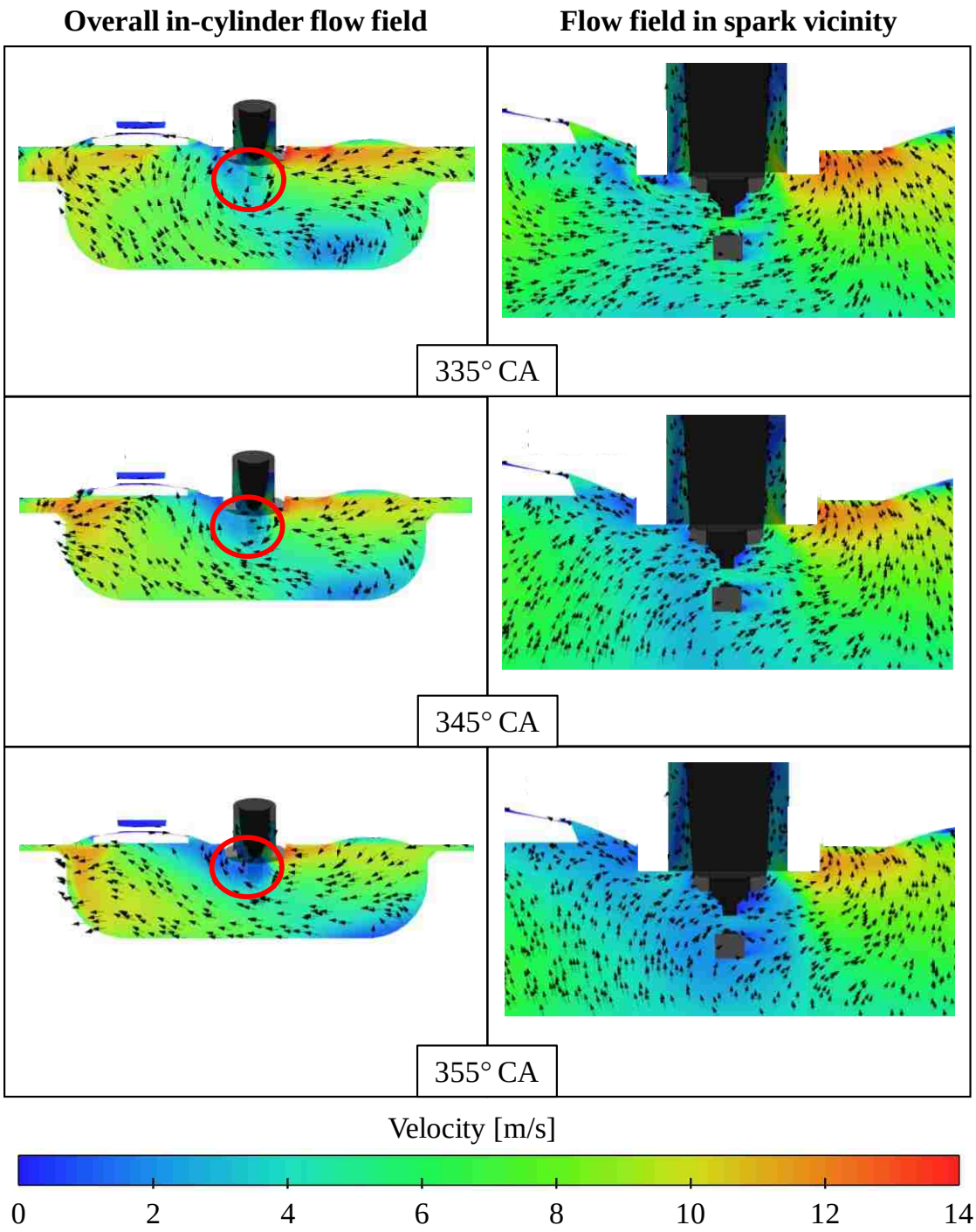

Figure 5-5. Overall in-cylinder and spark vicinity flow field at 5.56 g/s intake MAF

5.2 Spark Discharge Characteristics During Engine Motoring

The engine test platform and measurement equipment have previously been detailed in Chapter 3. A charging duration of 4 ms is used for the ignition coils of the TCI system. The breakdown voltage, the discharge duration, and the restrike frequency is calculated from the measured voltage and current profiles. The absolute value of the breakdown voltage may be higher than the value measured using the voltage probe. The time scale of the breakdown event is smaller than the sampling interval of the probe used. However, the measured values can be used for the comparison of the breakdown event at different spark timings. The discharge energy is calculated to be ~80 mJ for the spark events.

The breakdown voltage along with the in-cylinder pressure trace for different MAF conditions during the ignition window is presented in Figure 5-6. The breakdown voltage increases with the increase in the in-cylinder pressure as the piston moves towards TDC. However, there is no significant difference observed in the breakdown voltage values when the intake MAF is increased. This is expected as the pressure differences between the tested mass flow rates are not significant enough to alter the breakdown characteristics to a noticeable extent. Additionally, as demonstrated by the steady flow results, the flow velocity has a negligible effect on the breakdown process.

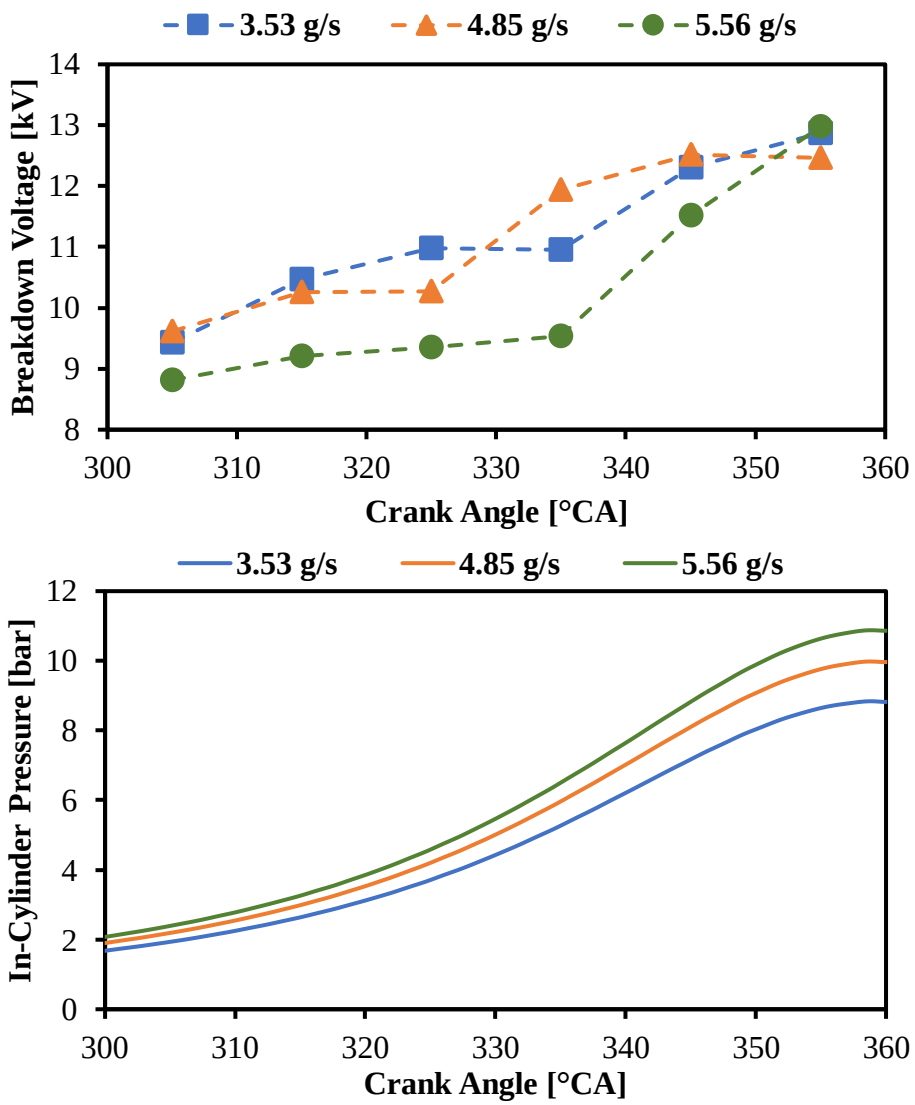

Figure 5-6. Breakdown voltage and in-cylinder pressure at different intake MAF

The glow phase of the discharge process is much more sensitive towards the effects of the flow velocity. As illustrated in Figure 5-7, the discharge duration initially decreases as the flow velocity increases. Further, the discharge duration then gradually increases as the flow velocity decreases near the TDC. The restrike frequency of the spark events is presented in Figure 5-8. The restrike frequency increases as the velocity increases and then gradually decreases.

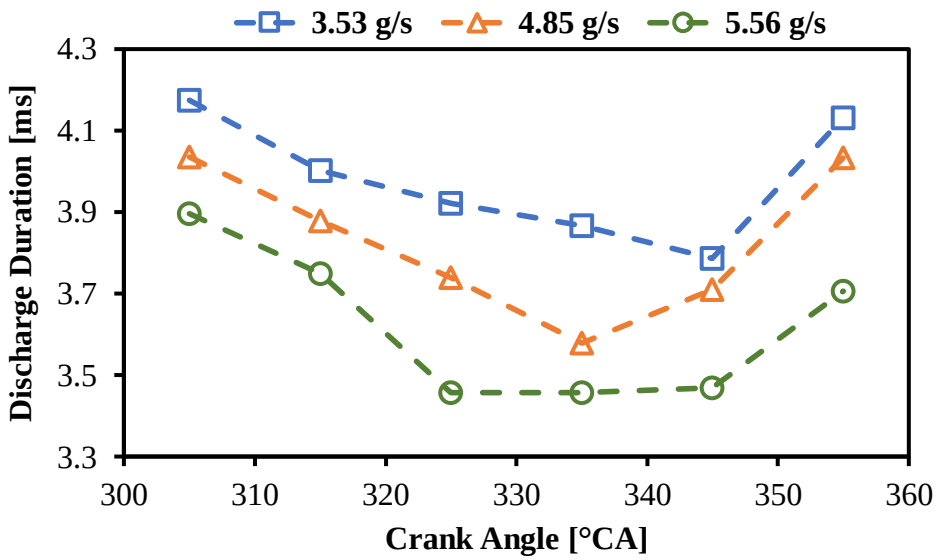

Figure 5-7. Discharge duration during of spark events at different intake MAF

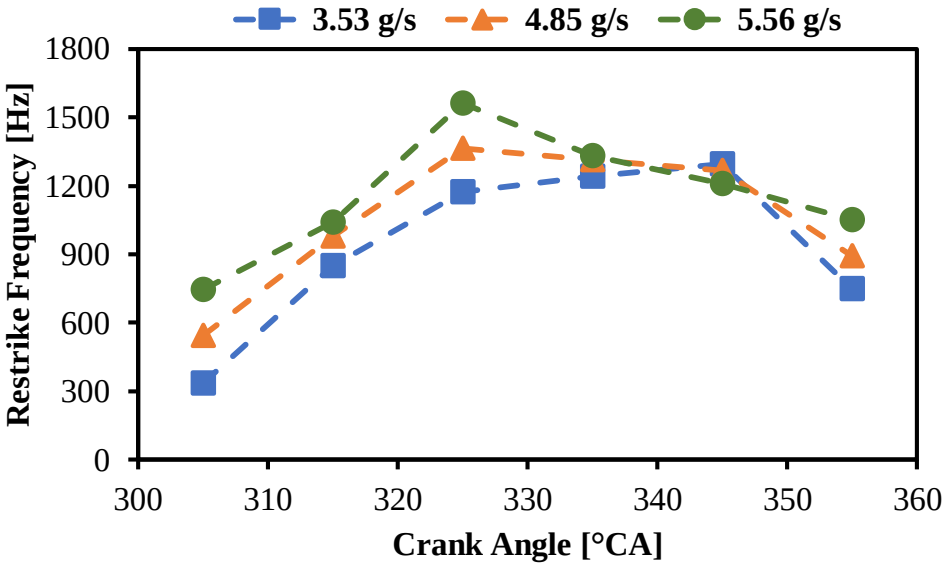

Figure 5-8. Restrike frequency of spark events at different intake MAF

Although the overall trend in the discharge duration and restrike frequency matches the variation in the velocity, the magnitude of the variation cannot be estimated from either the discharge duration or the restrike frequency. Only a qualitative correlation can be established. A possible reason for the discrepancy is the changes to the background pressure during the compression stroke. For this analysis, the effect of the background

pressure has not been considered. A “pressure correction” to the discharge characteristics may result in a better prediction of the flow velocity changes. After the pressure correction, it is a reasonable assumption that the correlation will hold true for the engine operation with combustion as well [55].

The results demonstrate that a similar correlation exists between flow velocity and the spark discharge characteristics under ambient as well as engine operating conditions. Thus, the spark anemometry can provide an economical and simple way of estimating the velocity variations near the spark gap, especially across different engine cycles (i.e. Cyclic variations) [41]. However, the velocity measurements can only be obtained during the spark event, therefore transient measurements are not possible using the conventional TCI system. Additionally, spark anemometry can only estimate the magnitude of the flow velocity. The information about the flow direction and turbulence cannot be obtained. Moreover, the flow within the engine cylinder is subject to constant variations and may not always resemble the cross-flow configuration, thereby further increasing the measurement uncertainty. The measurement interval may be prolonged by combining the spark anemometry with advanced ignition technologies that provide longer overall discharge duration e.g. dual-coil offset discharge [65].

CONCLUSIONS AND FUTURE WORK

An investigation on the effect of flow velocity on the flow field in the vicinity of the spark gap, and the spark discharge characteristics, was conducted using various research platforms and numerical simulations. The turbulence generated due to the spark plug geometry, and the spark discharge characteristics, were analyzed under steady cross flow tests. The use of spark anemometry to measure the variations in the flow velocity within the spark gap during engine operation was examined. In this chapter, the summary of the research performed is presented, along with the major conclusions. Thereafter, the recommendations for the future research are made.

6.1 Spark Discharge Under Steady Flow Conditions

The flow field around the spark plug, subjected to a steady flow across the spark gap was investigated using a combination of optical PIV measurements and numerical simulations. The turbulence generated by the spark geometry was studied. The discharge characteristics of the spark under various cross-flow velocities were investigated empirically in order to study the spark plasma response towards the flow field. The main conclusions of the research are as follows:

- The particle image velocimetry (PIV) system devised using a continuous laser can capture the overall flow field in the wake of the spark plug under relatively low mean flow velocities (up to 5 m/s). Larger flow structures are observed corresponding to the spark plug protrusions. However, reflections from the spark electrodes impede the flow field measurements within the spark gap.

- The spark plug geometry acts as bluff body, by which turbulence is generated in its wake. The turbulence is maximum downstream of the spark gap region. As the flow moves away downstream of the spark gap, the turbulence gradually dissipates.
- The flow velocity within the spark gap is higher than the mean stream velocity because of the contraction provided by the spark electrodes. A velocity gradient exists downstream of the spark gap. The flow velocity is lower in the regions following the obstruction provided by the spark plug geometry.
- Turbulence is lower within the spark gap as compared to the region after the spark electrodes.
- The flow velocity within the spark gap increases sharply with increase in mean flow velocity. The turbulent velocity and vorticity magnitudes show an almost linear rising trends with increases in mean flow velocity.
- Relatively low flow velocity and high turbulence downstream of the spark electrodes may provide better ignition and flame propagation conditions as compared to the gap region.
- The glow phase of spark discharge is more sensitive to the flow velocity variations than the spark breakdown phase. The breakdown voltage and peak current at the start of the glow phase remain constant over a testing range of velocities variations.
- During the glow phase, the spark plasma is stretched out of the spark gap and is subject to frequent restrikes under the effect of flow. At the same discharge current levels, the plasma stretched length and the restrike frequency increase with the increases in mean flow velocity. The restrikes may interrupt the formation of a self-

sustaining flame kernel, and present challenges to the ignition process at higher flow velocities.

- The total discharge duration decreases with an increase in mean flow velocity because of the additional energy dissipation during the restrike events.
- As the mean flow velocity increases, the onset of restrike events (first restrike) occurs closer to the breakdown phase, at a higher current level.

6.2 Spark Anemometry

A preliminary investigation on the use of spark anemometry to measure the variations in the local flow velocity during engine operation was conducted with the help of numerical simulations. Efforts have been made to correlate the simulation with the discharge voltage and current measurements on engine test platform. The in-cylinder flow field was analyzed using numerical simulations. The discharge characteristics namely breakdown voltage, discharge duration and restrike frequency were used to estimate the in-cylinder flow velocity changes in the spark gap. The main conclusions of the study are as follows:

- The overall in-cylinder tumble or swirl motion has a significant effect on the local flow field near the spark plug. The flow velocity in the spark gap decreases as the piston approaches the TDC because of the transformation of the tumble motion in part, as a result of the squish effect.
- The discharge duration and restrike frequency trends show a responsive agreement to the flow velocity variations in the spark gap. The spark anemometry is useful to give a qualitative estimate of the velocity variations. However, the magnitude of variations may not be obtained from the electrical measurements alone.

6.3 Recommendations for future work

The following are recommendations for the continuation of the future work related to the presented research:

- Optical measurements of the flow field due to spark plug geometry at higher mean flow velocity and background pressure should be performed in order to have a better relevance to the in-cylinder conditions.
- Spark discharge characteristics should be investigated under higher background pressure and different gas compositions to simulate the in-cylinder conditions during engine operation.
- Combustion tests under flow conditions must be performed to better understand the effects of generated turbulence and spark behavior on the flame kernel development and propagation.
- The simulated in-cylinder flow field has been validated only using the gas exchange process. Further validation of numerical results should be performed using velocity measurement methods to check the fidelity of the numerical model. Optical studies may help yield more information.

REFERENCES

1. U.S. EPA, “Light-Duty Automotive Technology, Carbon Dioxide Emissions, and Fuel Economy Trends: 1975 through 2017,” 2018.
2. Yang, Z., and Bandivadekar, A., “2017 Global Update: Light-Duty Vehicle Greenhouse Gas and Fuel Economy Standards,” The International Council on Clean Transportation, 2017.
3. United States Environmental Protection Agency, “EPA Emission Standards for Light-Duty Vehicles and Trucks,” Accessed from https://www.epa.gov/emission-standards-reference-guide/epa-emission-standards-light-duty-vehicles-and-trucks, November 18 2018.
4. Feng, A., Earley, R., And Green-Weiskel, L., “Global Overview on Fuel Efficiency and Motor Vehicle Emission Standards: Policy Options and Perspectives for International Cooperation,” N.D., 24, 2011.
5. “US: Light-Duty Fuel Economy and GHG,” Accessed from http://www.transportpolicy.net/standard/us-light-duty-fuel-economy-and-ghg/, November 18 2018.
6. “Trump Administration Proposes Freezing Fuel Economy Standards,” Accessed from https://www.npr.org/2018/08/02/634882047/trump-administration-proposes-freezing-fuel-economy-standards, November 18 2018.
7. Yu, S., Zheng, M., “Advanced Ignition System for Future Clean Combustion Engines: Review,” Journal of Automotive Safety and Energy, Vol.6 No.4, 2015.

8. Costagliola, M.A., De Simio, L., Iannaccone, S., and Prati, M.V., “Combustion efficiency and engine out emissions of a S.I. engine fueled with alcohol/gasoline blends,” Applied Energy 111:1162–1171, 2013.
9. Shiao, Y. and Dat, L.V., “Efficiency improvement for an unthrottled SI engine at part load,” International Journal of Automotive Technology 13(6):885–893, 2012.
10. Fekete, N., Gruden, I., Voigtländer, D., Nester, U., Krutzsch, B., Willand, J., and Kühn, M., “Advanced Engine Control and Exhaust Gas Aftertreatment of a Leanburn SI Engine,” SAE Transactions 106:1094–1103, 1997.
11. Ivanič, Ž., Ayala, F., Goldwitz, J., and Heywood, J.B., “Effects of Hydrogen Enhancement on Efficiency and NOx Emissions of Lean and EGR-Diluted Mixtures in a SI Engine,” SAE Technical Paper 2005-01–0253, 2005.
12. Stein, R.A., Anderson, J.E., and Wallington, T.J., “An Overview of the Effects of Ethanol-Gasoline Blends on SI Engine Performance, Fuel Efficiency, and Emissions,” SAE International Journal of Engines 6(1):470–487, 2013.
13. Germane, G.J., Wood, C.G., and Hess, C.C., “Lean Combustion in Spark-Ignited Internal Combustion Engines - A Review,” SAE Technical Paper 831694, 1983.
14. Attard, W.P. and Blaxill, H., “A Lean Burn Gasoline Fueled Pre-Chamber Jet Ignition Combustion System Achieving High Efficiency and Low NOx at Part Load,” SAE Technical Paper 2012-01-1146, 2012.
15. Wei, H., Zhu, T., Shu, G., Tan, L. et al., “Gasoline engine exhaust gas recirculation – A review,” Applied Energy 99:534–544, 2012.
16. Diana, S., Giglio, V., Iorio, B., and Police, G., “A Strategy to Improve the Efficiency of Stoichiometric Spark Ignition Engines,” SAE Technical Paper 961953, 1996.

17. Takahashi, D., Nakata, K., Yoshihara, Y. et al., “Combustion Development to Achieve Engine Thermal Efficiency of 40% for Hybrid Vehicles,” SAE Technical Paper 2015-01-1254, 2015.
18. Nakata, K., Nogawa, S., Takahashi, D., Yoshihara, Y. et al., "Engine Technologies for Achieving 45% Thermal Efficiency of S.I. Engine," SAE International Journal of Engines 9(1):179-192, 2016.
19. John, J., "Lean Burn Engine Concepts-Emissions and Economy," SAE Technical Paper 750930, 1975.
20. Kuo, T.-W., “What Causes Slower Flame Propagation in the Lean-Combustion Engine?,” Journal of Engineering for Gas Turbines and Power 112(3):348–356, 1990.
21. Ives, M., “Enhancement of Intake Generated Swirl to Improve Lean Combustion,” Electronic Theses and Dissertations 7364, 2017.
22. Heywood, J.B., “Internal Combustion Engine Fundamentals”, McGraw-Hill Co, Singapore, ISBN 13: 9780070286375, 1988.
23. Stone, R., “Introduction to Internal Combustion Engines”, SAE International, Warrendale, PA, ISBN-13: 9780768020847, 2012.
24. Mann, K.R.C., Ting, D.S.-K., and Henshaw, P.F., “A Semi-Empirical Model of Spark-Ignited Turbulent Flame Growth,” SAE Technical Paper 2000-01–0201, 2000.
25. Dev, S., "An Investigation of Premixed and Lean Combustion in Engines," Electronic Theses and Dissertations 7513, 2018.
26. Halldin, C., “Velocity and Turbulence Measurements Close to a Spark Plug,” SAE Technical Paper 920154, 1992.

27. Zheng, M., Gao, T., Jeftic, M., Han, X. et al., “A Preliminary Study of the Spark Characteristics for Unconventional Cylinder Charge with Strong Air Movement,” ASME. Internal Combustion Engine Division Fall Technical Conference, 461–470, 2011.
28. Yu, X., Yang, Z., Yu, S., Ives, M. et al., “Discharge Characteristics of Current Boosted Spark Events Under Flow Conditions,” ASME. Internal Combustion Engine Division Fall Technical Conference, Volume 1: Large Bore Engines; Fuels; Advanced Combustion: V001T03A017, 2017.
29. Sayama, S., Kinoshita, M., Mandokoro, Y., and Fuyuto, T., “Spark ignition and early flame development of lean mixtures under high-velocity flow conditions: An experimental study,” International Journal of Engine Research 1468087417748517, 2018.
30. Masuda, R., Sayama, S., Fuyuto, T., Nagaoka, M., Sugiura, A., and Noguchi, Y., “Application of Models of Short Circuits and Blow-Outs of Spark Channels under High-Velocity Flow Conditions to Spark Ignition Simulation,” SAE Technical Paper 2018-01–1727, 2018.
31. Schneider, A., Leick, P., Hettinger, A., and Rottengruber, H., “Experimental studies on spark stability in an optical combustion vessel under flowing conditions,” in: Liebl, J. and Beidl, C., eds., Internationaler Motorenkongress 2016, Springer Fachmedien Wiesbaden, ISBN 978-3-658-12918-7: 327–348, 2016.
32. Brandt, M., Hettinger, A., Schneider, A., Senftleben, H., et al., “Extension of Operating Window for Modern Combustion Systems by High Performance Ignition,”

Ignition Systems for Gasoline Engines, Springer International Publishing, ISBN 978-3-319-45504-4: 26–51, 2017.

33. Schild, I.B., “Influence of Spark Energy, Spark Number, and Flow Velocity on Detonation Initiation in a Hydrocarbon-fueled PDE,” Thesis, Georgia Institute of Technology, 2005
34. Herweg, R., Begleris, P., Zettlitz, A., and Ziegler, G.F.W., “Flow Field Effects on Flame Kernel Formation in a Spark-Ignition Engine,” SAE Transactions 97:826–846, 1988.
35. Witze, P.O., Martin, J.K., and Borgnakke, C., “Conditionally-Sampled Velocity and Turbulence Measurements in a Spark Ignition Engine,” Combustion Science and Technology 36(5–6):301–317, 1984.
36. Adrian, R.J. and Westerweel, J., “Particle Image Velocimetry,” Cambridge University Press, ISBN 978-0-521-44008-0, 2011.
37. Adrian, R.J., “Twenty years of particle image velocimetry,” Experiments in Fluids 39(2):159–169, 2005.
38. “Particle Image Velocimetry (PIV) Measurement Principles,” Accessed from https://www.dantecdynamics.com/measurement-principles-of-piv, November 18 2018.
39. LaVision, “Flowmaster manual,” Accessed from https://www.lavision.de/en/products/flowmaster , November 18 2018.
40. “How Frame-Straddling Works,” Accessed from http://www.tsi.com/uploadedFiles/_Site_Root/Products/Literature/Technical_Notes/How%20Frame-Straddling%20Works.pdf, Novermber 18 2018.

41. Kim, J. and Anderson, R.W., “Spark Anemometry of Bulk Gas Velocity at the Plug Gap of a Firing Engine,” SAE Technical Paper 952459, 1995.
42. Hall, M.J., Bracco, F.V., and Santavicca, D.A., “Cycle-Resolved Velocity and Turbulence Measurements in an IC Engine with Combustion,” SAE Technical Paper 860320, 1986.
43. Spicher, U. and VeIji, A., “Measurements of Spatial Flame Propagation and Flow Velocities in a Spark Ignition Engine,” 20th Symposium on Combustion Ann Arbor, August 12-17, 1984.
44. Kyriakides, S. C. and Glover, A. R., “A study of the correlation between in-cylinder air motion and combustion in gasoline engines” Institute of Mechanical Engineers C55/88, 1988.
45. Arcoumanis, C. and Bae, C.-S., “Visualization of Flow/Flame Interaction in a Constant-Volume Combustion Chamber,” SAE Technical Paper, 1993.
46. Dulger, M., Sher, E., "Experimental Study on Spark Ignition of Flowing Combustible Mixtures", SAE Technical Paper 951004, 1995.
47. Rivin, B., Dulger, M., and Sher, E., “Extending Lean Misfire Limit of Methane-Air Mixtures by Means of an Enhanced Spark Discharge,” SAE Technical Paper 1999-01–0573, 1999.
48. Ballal, D.R. and Lefebvre, A.H., “The influence of spark discharge characteristics on minimum ignition energy in flowing gases,” Combustion and Flame 24, 1975.
49. Johansson, B., “Cycle to Cycle Variations in S.I. Engines - The Effects of Fluid Flow and Gas Composition in the Vicinity of the Spark Plug on Early Combustion,” SAE Technical Paper 962084, 1996.

50. Aleiferis, P.G., Taylor, A.M.K.P., Whitelaw, J.H., Ishii, K., and Urata, Y., "Cyclic Variations of Initial Flame Kernel Growth in a Honda VTEC-E Lean-Burn Spark-Ignition Engine," SAE Technical Paper 2000-01–1207, 2000.
51. Lindvall, F. C., "A Glow Discharge Anemometer," Transactions of American Institute of Electrical Engineers, 53, 1063–1073, 1934.
52. Maly, R., and Meinel, H., "Determination of Flow Velocity, Turbulence Intensity and Length and Time Scales from Gas Discharge Parameters," Proceedings of the Fifth International Symposium on Plasma Chemical, Vol. ISPC-5, pp. 552–557, 1981.
53. Maly, R., Meinel, H., and Wagner, E., "Novel Method for Determining General Flow Parameters from Conventional Spark Discharge," Institute of Mechanical Engineers Conference Transactions, C67/83, pp. 27–32, 1985.
54. Pashley, N., Stone, R., and Roberts, G., "Ignition System Measurement Techniques and Correlations for Breakdown and Arc Voltages and Currents," SAE Technical Paper 2000-01–0245, 2000.
55. Gardiner, D.P., Wang, G., Bardon, M.F., LaViolette, M. et al., "An Experimental Study of Spark Anemometry for In-Cylinder Velocity Measurements," ASME. Internal Combustion Engine Division Fall Technical Conference, ASME 2006 Internal Combustion Engine Division Fall Technical Conference (ICEF2006), 393–404, 2006.
56. International Organization for Standardization, "ISO-5167 Standard, "Measurement of Fluid Flow by Means of Pressure Differential Devices Inserted in Circular Cross-

Section Conduits Running Full – Part 1: General Principles and Requirements", ISO 5167-1:2003, 2003.

57. Melling, A., "Tracer particles and seeding for particle image velocimetry," Measurement Science and Technology 8(12):1406, 1997.
58. Echols, W.H., and Young, Y.A., "Studies of portable air-operated aerosol generators," NRL Report 5929, Naval Research Laboratory, Washington, D.C., 1963.
59. Tropea, C. and Yarin, A.L., "Springer Handbook of Experimental Fluid Mechanics," Springer Science & Business Media, ISBN 978-3-540-25141-5, 2007.
60. Kähler, C.J., Sammler, B., and Kompenhans, J., "Gneeration and Control of Particle Size Distributions for Optical Velocity Measurement Techniques in Fluid Mechanics," 4th International Symposium On PIV, Göttingen, Germany, September 17-19, 2001.
61. Thielicke, W. and Stamhuis, E., "PIVlab – Towards User-friendly, Affordable and Accurate Digital Particle Image Velocimetry in MATLAB," Journal of Open Research Software 2(1):e30, 2014.
62. Converge CFD, "ConvergeCFD Manual Series – Converge Manual 2.3", 2016.
63. Halldin, C., "Influence of the inlet turbulence on the flow field downstream a sudden expansion: Comparison between calculations and LDV-measured data," Lund University LUTMDN/(TMVK-7006)/1-89, 1990 (in Swedish).
64. White, F.M., "Fluid Mechanics," McGraw Hill, ISBN 978-0-07-352934-9, 2011.
65. Zhu, H., "Spark Energy and Transfer Efficiency Analyses on Various Transistor Coil Ignition Systems," Electronic Theses and Dissertations 7456, 2018.

LIST OF PUBLICATIONS

1. Sandhu, N., Dev, S., Purohit, D., Yang, Z., Zheng, M., Ting, D., “Preliminary Simulation Study of Flow Field around a Spark Plug under Ambient and Engine Conditions,” The Energy Mix for Sustaining our Future, 2018.
2. Dev, S., Sandhu, N. S., Ives, M., Yu, S., Zheng, M., Tjong, J., “Ion Current Measurement of Diluted Combustion Using a Multi-Electrode Spark Plug,” SAE Technical Paper 2018-01-1134, 2018.
3. Purohit, D., Dev, S., Aversa, C., Sandhu, N.S., and Zheng, M., “Impact of Alternative Fuels on the Performance of a Long Breathing Lean NOx Trap,” Combustion Institute – Canadian Section Spring Technical Meeting, Toronto, May 14-17, 2018.

VITA AUCTORIS

NAME:	Navjot Singh Sandhu
PLACE OF BIRTH:	Amritsar, Punjab, India
YEAR OF BIRTH:	1991
EDUCATION:	B.E. – Mechanical Engineering BITS - Pilani 2010-2014
	M.A.Sc. Mechanical Engineering University of Windsor 2016-2018